JACS
JOURNAL OF THE AMERICAN CHEMICAL SOCIETY
Article
pubs.acs.org/JACS

On the Magnetic and Spectroscopic Properties of High-Valent Mn_3CaO_4 Cubanes as Structural Units of Natural and Artificial Water-Oxidizing Catalysts

Vera Krewald, Frank Neese, and Dimitrios A. Pantazis*

Max Planck Institute for Chemical Energy Conversion, Stiftstrasse 34−38, 45470 Mülheim an der Ruhr, Germany

Supporting Information

ABSTRACT: The $Mn(IV)_3CaO_4$ cubane is a structural motif present in the oxygen-evolving complex (OEC) of photosystem II and in water-oxidizing Mn/Ca layered oxides. This work investigates the magnetic and spectroscopic properties of two recently synthesized complexes and a series of idealized models that incorporate this structural unit. Magnetic interactions, accessible spin states, and ^{55}Mn isotropic hyperfine couplings are computed with quantum chemical methods and form the basis for structure−property correlations. Additionally, the effects of oxo-bridge protonation and one-electron reduction are examined. The calculated properties are found to be in excellent agreement with available experimental data. It is established that all synthetic and model $Mn(IV)_3CaO_4$ cubane complexes have the same high-spin $S = {}^9/_2$ ground state. The magnetic coupling conditions under which different ground spin states can be accessed are determined. Substitution of Mn(IV) magnetic centers by diamagnetic ions [e.g., Ge(IV)] allows one to "switch off" specific spin sites in order to examine the magnetic orbitals along individual Mn−Mn exchange pathways, which confirms the predominance of ferromagnetic interactions within the cubane framework. The span of the Heisenberg spin ladder is found to correlate inversely with the number of protonated oxo bridges. Energetic comparisons for protonated models show that the tris-μ-oxo bridge connecting only Mn ions in the cubane has the lowest proton affinity and that the average relaxation energy per additional proton is on the order of 18 kcal·mol^{-1}, thus making access to ground states other than the high-spin $S = {}^9/_2$ state in these cubanes unlikely. The relevance of these cubanes for the OEC and synthetic oxides is discussed.

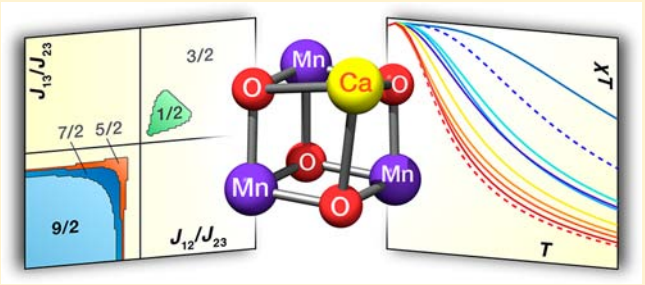

1. INTRODUCTION

Research into the synthesis and properties of oligonuclear manganese complexes over the last few decades has created one of the richest and most diverse fields of inorganic chemistry. A large part of this research effort is being driven by the central role of manganese in the catalysis of the most important biological reaction for aerobic life on our planet, the oxidation of water by the enzyme photosystem II (PS-II) of photosynthetic organisms.[1−3] This reaction is the foundation for all envisioned solar-fuel-based sustainable energy scenarios; hence the natural system is the obvious starting point for any bioinspired approach.[4−7]

The active site of PS-II, known as the oxygen-evolving complex (OEC), consists of a protein-embedded evolutionarily conserved inorganic core that cycles through five oxidation states (the S states of the Kok cycle,[8] S_0−S_4) to perform the four-electron oxidation of water. The OEC is a heterometallic cluster unique in biology: it contains four manganese ions and one calcium ion, which was shown to be an essential cofactor long before the structure of the OEC was elucidated.[9] It is now established that Ca^{2+} is part of the active-site Mn_4CaO_5 core. The recent X-ray diffraction (XRD) model of PS-II at 1.9 Å resolution[10] offers the clearest view so far of the metal ion positions. According to this model, the inorganic core of the OEC contains a cuboidal Mn_3CaO_4 unit, with which the fourth Mn ion is associated via a corner-oxo attachment and an additional μ-oxo bridge. The bonding topology and the precise positions of the oxo bridges are still debatable owing to X-ray-induced reduction and to the inherent flexibility of the OEC.[11−15] However, spectroscopic and computational evidence do suggest that a cuboidal $Mn(IV)_3CaO_4$ subunit is present in one of two interconvertible structural forms that exist in the S_2 state of the Kok cycle (Figure 1).[15] Thus, whether a persistent feature or not, the properties of such a unit are of major importance in understanding the structure−function relationships in the OEC.

Besides this enzymatic site, the synergy between manganese and calcium for water oxidation is encountered in the quite different setting of heterogeneous catalysis. Synthetic layered Mn/Ca oxides belonging to the birnessite family of manganese minerals were shown to be highly active catalysts for the oxidation of water.[16−19] Extended X-ray absorption fine structure (EXAFS) studies indicated the presence of

Received: December 23, 2012
Published: March 25, 2013

   dx.doi.org/10.1021/ja312552f | J. Am. Chem. Soc. 2013, 135, 5726−5739

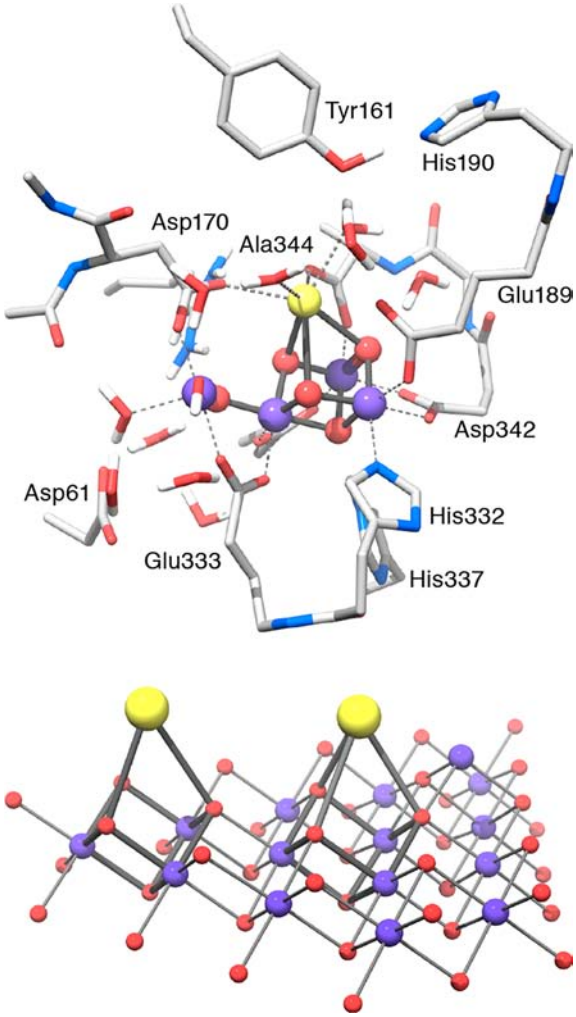

Figure 1. (Top) One of two possible structural forms of the OEC core at the S_2 state[15] (most hydrogen atoms have been omitted for clarity). (Bottom) Hypothetical structural model for catalytically active Mn/Ca layered oxides.[16]

Mn_3CaO_4 cubane units in these oxides, along with a large number of Mn vacancies (Figure 1).[19] Even though water oxidation by manganese oxides may be achieved without a strict requirement for Ca^{2+},[20] the above observations suggest that the Mn_3CaO_4 motif is relevant to all forms and scales of Mn-based water oxidation chemistry.

The final steps of water oxidation in the OEC are realized through access to high manganese oxidation states, that is, Mn(III) and higher. According to some proposals, these may reach formally up to Mn(V) for one of the ions prior to O−O bond formation.[21,22] There is general, but not complete,[23−25] consensus that three Mn(IV) and one Mn(III) ions are present in the S_2 state of the Kok cycle, while all ions may be Mn(IV) in the S_3 state if no ligand-based oxidation[26] occurs in the S_2−S_3 transition. In striking analogy with the natural system, Zaharieva et al.[19] demonstrated that Mn(IV) ions comprise around 80% of manganese in the catalytically active synthetic Mn/Ca oxides, with the remainder attributed to Mn(III). On that basis, Mn(IV) is expected to be the dominant oxidation state in both biological and solid-state catalytic systems.

Attempts to synthesize high oxidation state Mn/Ca compounds have typically resulted in complexes that either have higher nuclearity than the OEC or—with the exception of a tridecamanganese cluster[27]—simply lack a cuboidal Mn_3CaO_4 unit.[27−31] This had so far obstructed the study of the cubane motif per se. However, recent synthetic efforts by Agapie and co-workers[32] and Christou and co-workers[33] led to the first well-defined $Mn(IV)_3CaO_4$ complexes. Both were crystallographically characterized and studied by a range of methods, including magnetic susceptibility studies, electron paramagnetic resonance (EPR), electron nuclear double resonance (ENDOR), and X-ray absorption spectroscopies for the complex of Christou and co-workers (**1**)[33] and cyclic voltammetry for that of Agapie and co-workers (**2**).[32] As shown in Figure 2, complex **1** contains a $Mn(IV)_3Ca_2O_4$ core with carboxylate and carboxylic acid ligands, where a second Ca^{2+} ion is attached to the Mn_3CaO_4 cubane via an oxo bridge. On the other hand, **2** contains a $Mn(IV)_3CaO_4$ core with a unique ligand framework built around a 1,3,5-triarylbenzene spacer and incorporates six pyridine and three alcohol groups. Additionally, three acetato ligands bridge Ca^{2+} with each of the Mn ions and a tetrahydrofuran molecule completes the coordination sphere of Ca^{2+}.

These complexes have a strong structural resemblance to the OEC, with the advantage of being of intermediate complexity between the well-understood binuclear complexes and the natural system. Thus, they offer an ideal platform to investigate intrinsic properties of the Mn_3CaO_4 cubane unit, while avoiding the complications inherent in the study of the OEC. At the same time, they offer the possibility to study an integral component of the Mn/Ca oxides while retaining the ability to apply high-level electronic structure and property prediction methods.

From a theoretical perspective, high oxidation state manganese dimers with various bridging motifs have been studied extensively in the past two decades with respect to their magnetic and, more recently, their spectroscopic properties.[34−44] These studies have contributed significantly in advancing our understanding of the magnetic and spectroscopic data of exchange-coupled manganese systems in general and the OEC in particular, since such dimeric motifs can be considered subunits of the catalytic site. Similar computational studies on manganese compounds of higher nuclearity are less common,[45−51] owing in part to the increased size and complexity of the systems but also to the paucity of reference-quality data for a variety of properties.

In this work we study the geometric and electronic structure and magnetic and selected spectroscopic properties of complexes **1** and **2**, in comparison with experimental data. A series of questions relevant to functional aspects of the catalytic systems are also addressed, including the effects of oxo-bridge protonation on magnetic properties and EPR parameters, the effect of redox-state changes, and the role of Ca^{2+}. Finally, we review the intrinsic properties of Mn_3CaO_4 cubanes in relation to synthetically accessible ground spin states, explore the links with the phenomenology of the OEC, and discuss the implications for existing water oxidizing catalysts.

2. METHODOLOGY

2.1. Magnetochemistry. The complexes studied in this work comprise three Mn(IV) ions with local high-spin isotropic d^3 electronic configurations in quasi-octahedral ligand environments. Treating them as magnetically coupled systems involves three spin operators $\hat{\mathbf{S}}_1 = \hat{\mathbf{S}}_2 = \hat{\mathbf{S}}_3$ representing the ions, each with spin quantum number $S = {}^3/_2$ and magnetic quantum numbers $M_S = +{}^3/_2, +{}^1/_2, -{}^1/_2$, and $-{}^3/_2$. Angular momentum algebra can be used to obtain a total $\hat{\mathbf{S}}_T$

dx.doi.org/10.1021/ja312552f | J. Am. Chem. Soc. 2013, 135, 5726−5739

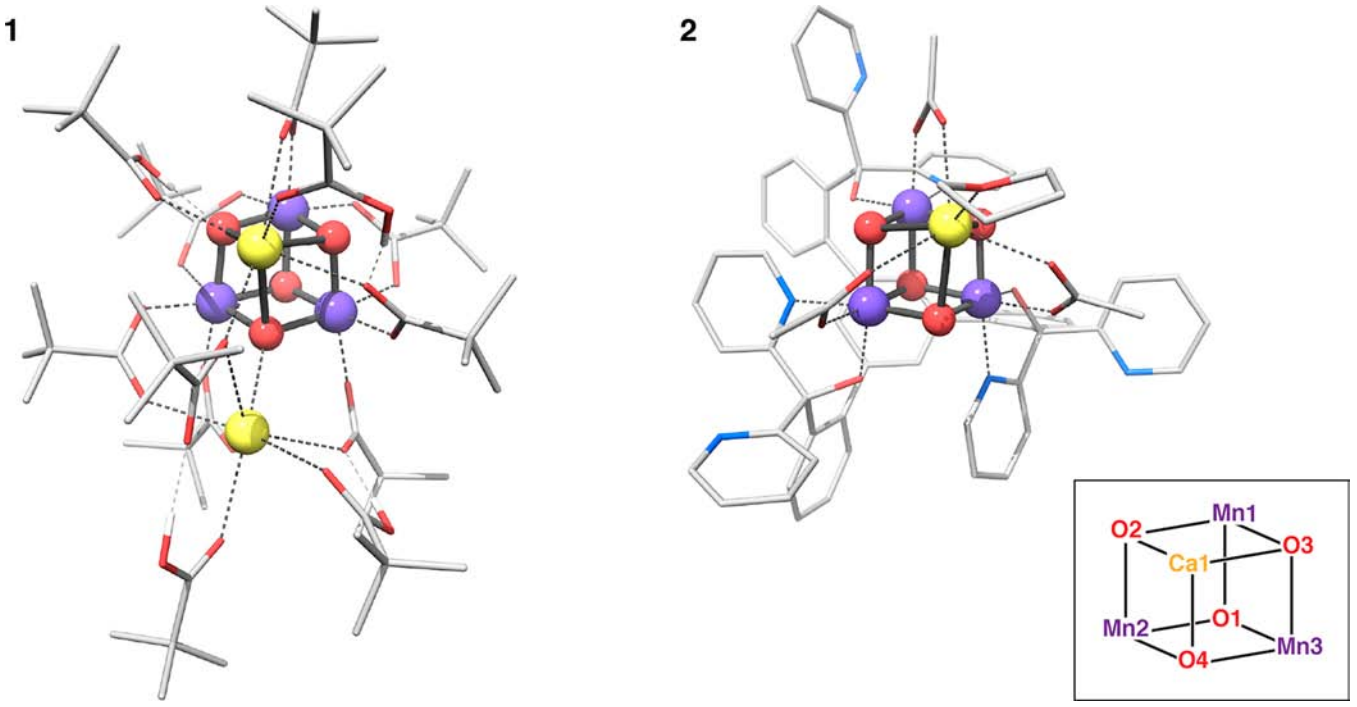

Figure 2. Geometry-optimized structures of complexes **1** and **2**, incorporating the $Mn(IV)_3CaO_4$ cubane core. Hydrogen atoms that do not participate in hydrogen bonds have been omitted for clarity. The common labeling scheme shown in the inset is used throughout this paper.

$= \hat{\mathbf{S}}_1 + \hat{\mathbf{S}}_2 + \hat{\mathbf{S}}_3$. The spins are coupled sequentially, with the first two producing $\hat{\mathbf{S}}_{12} = \hat{\mathbf{S}}_1 + \hat{\mathbf{S}}_2$ with spin quantum numbers $S_{12} = S_1 + S_2, S_1 + S_2 - 1, ..., {}^1/_2$, or 0. In the present case S_{12} takes the values 3, 2, 1, and 0. This is coupled with the third operator to produce $\hat{\mathbf{S}}_T = \hat{\mathbf{S}}_{12} + \hat{\mathbf{S}}_3$ with $S_T = S_{12} + S_3, S_{12} + S_3 - 1, ..., |S_{12} - S_3|$. Going over all S_{12} values, one obtains $S_T(S_{12} = 3) = {}^9/_2, {}^7/_2, {}^5/_2, {}^3/_2$; $S_T(S_{12} = 2) = {}^7/_2, {}^5/_2, {}^3/_2, {}^1/_2$; $S_T(S_{12} = 1) = {}^5/_2, {}^3/_2, {}^1/_2$; and $S_T(S_{12} = 0) = {}^3/_2$. Thus, the coupling of the three Mn(IV) ions generates 12 magnetic levels (multiplets), comprising 64 sublevels. The goal is to establish the order and energies of these levels, since they determine the observable properties such as magnetization and EPR parameters. Whether the relative energies of some or all levels are experimentally or theoretically obtained, the isotropic Heisenberg–Dirac–van Vleck (HDvV) Hamiltonian is used:

$$\hat{\mathbf{H}}_{\mathrm{HDvV}} = -2 \sum_{i<j} J_{ij} \hat{\mathbf{S}}_i \cdot \hat{\mathbf{S}}_j \tag{1}$$

where i and j denote the paramagnetic centers, or, for the present case:

$$\hat{\mathbf{H}}_{\mathrm{HDvV}} = -2J_{12} \hat{\mathbf{S}}_1 \cdot \hat{\mathbf{S}}_2 - 2J_{13} \hat{\mathbf{S}}_1 \cdot \hat{\mathbf{S}}_3 - 2J_{23} \hat{\mathbf{S}}_2 \cdot \hat{\mathbf{S}}_3 \tag{2}$$

Consistent with experiment and expectations, symmetric anisotropic contributions and antisymmetric (noncollinear) interactions can be ignored for the present complexes.[52,53] Furthermore, given the strong preference of Mn(IV) for a high-spin configuration in most relevant ligand fields, isotropic deviations due to non-Hund states[54] should play no role. All the information about the order and spacing of the spin levels is thus condensed into the isotropic exchange coupling constants J_{ij}. This information can be inferred, at least in part, from thermal depopulation experiments. In general, fitting the unknown J_{ij} constants to a set of measurements is an underdetermined problem[46] unless a sufficiently large number of energy levels is probed.

The general form of the Hamiltonian in eq 2 is used throughout this work, since no assumptions are made regarding the equivalence of magnetic exchange pathways. The observed magnetic properties of **1** were fitted in terms of an isosceles triangle with Mn1 at the apex,[33] that is, $J_{12} = J_{13} = J \neq J_{23}$. The Hamiltonian is then

$$\hat{\mathbf{H}}_{\mathrm{HDvV}} = -2J(\hat{\mathbf{S}}_1 \cdot \hat{\mathbf{S}}_2 + \hat{\mathbf{S}}_1 \cdot \hat{\mathbf{S}}_3) - 2J_{23} \hat{\mathbf{S}}_2 \cdot \hat{\mathbf{S}}_3 \tag{3}$$

For three equivalent pathways ($J_{12} = J_{13} = J_{23} = J$), this reduces further to

$$\hat{\mathbf{H}}_{\mathrm{HDvV}} = -2J(\hat{\mathbf{S}}_1 \cdot \hat{\mathbf{S}}_2 + \hat{\mathbf{S}}_1 \cdot \hat{\mathbf{S}}_3 + \hat{\mathbf{S}}_2 \cdot \hat{\mathbf{S}}_3) \tag{4}$$

which will be shown to be a good approximation for cubane **2**. Equation 3 can be solved analytically,[55] while in general the eigenvalues and eigenfunctions of $\hat{\mathbf{H}}_{\mathrm{HDvV}}$ are obtained by diagonalization.

All of the above is independent of electronic structure calculations. The spin-level energies can in principle be obtained by a theoretical method that properly treats spin eigenstates. However, although the problem is inherently multideterminantal (only the $S = {}^9/_2$ state is representable by a single determinant), the only pragmatic approach today is density functional theory (DFT)[56] within the broken symmetry (BS) formalism.[57−73] Moving from spin eigenfunctions to the set of BS determinants is equivalent to treating the spin coupling in terms of the Ising Hamiltonian

$$\hat{\mathbf{H}}_{\mathrm{Ising}} = -2 \sum_{i<j} J_{ij} \hat{S}_{z_i} \cdot \hat{S}_{z_j} \tag{5}$$

For each $\hat{S}_{z_i}$ in the present Mn(IV) systems, $M_{S_i} = +{}^3/_2$ or $-{}^3/_2$; hence, for the $Mn(IV)_3$ cubanes, there is one ferromagnetic (FM) solution with total $M_S = {}^9/_2$ and three BS solutions with total $M_S = {}^3/_2$ (excluding equivalent solutions with total $M_S < 0$). These may be represented in terms of individual M_{S_i} values as $|M_{S_1}, M_{S_2}, M_{S_3}; M_S\rangle$; that is, the possible solutions are FM = $|{}^3/_2, {}^3/_2, {}^3/_2; {}^9/_2\rangle$, $BS_1 = |-{}^3/_2, {}^3/_2, {}^3/_2; {}^3/_2\rangle$, $BS_2 = |{}^3/_2, -{}^3/_2, {}^3/_2; {}^3/_2\rangle$, and $BS_3 = |{}^3/_2, {}^3/_2, -{}^3/_2; {}^3/_2\rangle$. Attainment of the correct solution is confirmed by the sign and value of the spin populations, which deviate by less than 0.2 electron from the formal integer value of 3 for Mn(IV).

BS solutions with total $|M_S| \neq {}^3/_2$ are not part of the spin-coupling problem at hand. These can be obtained only by changing the electronic configuration of a Mn ion, defining a fundamentally different set of local spin operators. It is unsurprising that an $M_S = {}^1/_2$ BS solution can be tens of kilocalories per mole higher than the "proper" BS determinants.[74] Such solutions describe either (i) an electronic excitation to a spin-paired state, an extremely unfavorable event for a quasi-octahedral Mn(IV) ion, or (ii) a flipping of a 3d

dx.doi.org/10.1021/ja312552f | J. Am. Chem. Soc. 2013, 135, 5726−5739

electron that remains unpaired within the 3d manifold, invalidating the entire procedure by forming an S_z component that is not an eigenfunction of the local spin operators.[75] A clear warning sign would be a large spin population drop at a Mn center.

Since $\hat{\mathbf{H}}_{\mathrm{HDvV}}$ and $\hat{\mathbf{H}}_{\mathrm{Ising}}$ do not commute, a mapping procedure is required.[69] This rests on the fact that the J_{ij} constants are common for $\hat{\mathbf{H}}_{\mathrm{Ising}}$ and $\hat{\mathbf{H}}_{\mathrm{HDvV}}$, provided all electrons on each metal are of the same spin.[75] Hence, by transferring the BS-deduced J_{ij} values to $\hat{\mathbf{H}}_{\mathrm{HDvV}}$ and diagonalizing the latter, the full spectrum of energy levels is obtained. If the single-determinant energies are reasonably accurate, this procedure ensures that the correct ground state—and complete spin ladder—can be obtained regardless of its total spin. This has been demonstrated for a trinuclear Mn(IV) complex with an $S = {}^1/_2$ ground state.[47] For more than three spins, the problem is overdetermined and can be solved via singular value decomposition.[15,46,49,73,76−78]

2.2. Computational Details. The crystal structures[32,33] were used as starting points for geometry optimizations, carried out in the high-spin states. After testing of several density functionals (see Supporting Information), TPSS[79] was chosen for optimizations and TPSSh[80] for property calculations. Scalar relativistic effects were included with the zeroth-order regular approximation (ZORA)[81,82] retaining one-center terms and using ZORA-recontracted polarized triple-ζ basis sets.[83,84] Fully decontracted auxiliary basis sets were used for the resolution of identity (RI) and chain-of-spheres (COSX) approximations[85] to Coulomb and exact exchange, as implemented in ORCA.[86] A Lebedev 590 angular grid, increased integration accuracy, and tight convergence criteria were chosen. Grimme's D3 dispersion corrections were used.[87] One-electron reduction of the clusters and oxo-bridge protonation were studied with simplified models. The conductorlike screening model (COSMO),[88] with the assumption of a perfect conductor, was used for these systems to avoid artifacts arising from the high charge. Boltzmann populations were computed from energy levels obtained by diagonalization of $\hat{\mathbf{H}}_{\mathrm{HDvV}}$ by use of the ORCA module orca_eca. Magnetic susceptibilities were computed with the JulX program.[89] Calculations of ^{55}Mn hyperfine coupling constants (HFCs) followed established protocols (see Supporting Information).[40,46,49,76]

3. RESULTS ON SYNTHETIC CUBANES

3.1. Structures and Magnetism. The Mn1−Mn2 and Mn1−Mn3 distances in the XRD ($\mathbf{1}_{\mathrm{XRD}}$) and optimized structures ($\mathbf{1}_{\mathrm{opt}}$) of complex **1** are slightly shorter than the Mn2−Mn3 distance; the Mn−O−Mn angles involving Mn1 are more acute ($\mathbf{1}_{\mathrm{XRD}}$: 92.1°, 93.3°, 96.2°, and 96.8°) than those between Mn2 and Mn3 ($\mathbf{1}_{\mathrm{XRD}}$: 98.1° and 99.1°). In $\mathbf{1}_{\mathrm{opt}}$, the larger angles are underestimated by up to 0.8° and the smaller ones by 0.2° on average. Overall there is excellent agreement between $\mathbf{1}_{\mathrm{XRD}}$ and $\mathbf{1}_{\mathrm{opt}}$. Complex **2** is highly symmetric with similar Mn−Mn distances and all Mn−O4−Mn angles ∼95°. These features of the XRD structure are also accurately reproduced by the calculations.

In terms of electronic structure, the spin density is localized on the Mn ions, which carry 2.9−3.0 unpaired electrons, almost coinciding with the formal oxidation states. No significant spin density is found on the oxo bridges. The computed J values for **1** are consistent with the fitted values, with one moderately antiferromagnetic pathway and two ferromagnetic ones of medium magnitude (Table 2). For values computed at the experimental geometry ($\mathbf{1}_{\mathrm{XRD}}$), one of the positive Js is closer to the fitted value than the other, but the magnitude of the antiferromagnetic interaction is underestimated compared with the experimental fit, even for the $\mathbf{1}_{\mathrm{XRD}}$ model. The computational results for both $\mathbf{1}_{\mathrm{XRD}}$ and $\mathbf{1}_{\mathrm{opt}}$ suggest that the two pathways considered equivalent in the fitting are in fact different, and that a model with three inequivalent exchange couplings (eq 2) would be more appropriate for this system. It is noted, however, that fitting to thermal depopulation data can quickly become underdetermined for oligonuclear complexes when the energetic separation of the lowest energy levels is of the same magnitude as the thermal energy.[46]

Christou and co-workers[33] suggested that the negative J_{23} may be related to more obtuse Mn2−O−Mn3 angles caused by the external Ca^{2+}. Closer examination reveals that the antiferromagnetic interaction results from a combination of structural effects where the sterically demanding ^{t}Bu groups play an important role: their truncation to methyl groups and relaxation of the resulting structure leads to three ferromagnetic pathways, albeit with different magnitudes (7.6, 56.8, and 22.1 cm^{-1}). The effect is more pronounced for modification of the cubane to a structure with carboxylates coordinating the Mn ions on all cubane faces: this structure without the second Ca^{2+} has three ferromagnetic pathways (38.3, 41.3, and 37.7 cm^{-1}). Thus, the coordination mode of the carboxylates connecting Mn2 and Mn3 with the external Ca^{2+} introduces a structural flexibility that leads to a unique pathway, which may or may not be antiferromagnetic depending on other geometric factors such as proximal bulky groups.

The results for **1** confirm that the current approach gives good predictions for the magnetic couplings. In **2**, for which no similar data are available at present, all exchange pathways are predicted to be ferromagnetic and of similar strength, leading again to an $S = {}^9/_2$ ground state. The inequivalence of exchange couplings in $\mathbf{2}_{\mathrm{XRD}}$ reflects a structural asymmetry that is lost in

Table 1. Selected Interatomic Distances from Crystal Structures of 1 and 2 Compared with Optimized Values[a]

	$\mathbf{1}_{\mathrm{XRD}}$	$\mathbf{1}_{\mathrm{opt}}$	$\mathbf{2}_{\mathrm{XRD}}$	$\mathbf{2}_{\mathrm{opt}}$
Mn1−Mn2, Å	2.757	2.773	2.839	2.820
Mn1−Mn3, Å	2.730	2.726	2.833	2.820
Mn2−Mn3, Å	2.857	2.845	2.830	2.817
Mn1−Ca1, Å	3.394	3.477	3.231	3.315
Mn2−Ca1, Å	3.454	3.446	3.224	3.314
Mn3−Ca1, Å	3.418	3.435	3.238	3.318
Mn1−O1, Å	1.899	1.920	1.916	1.923
Mn1−O2, Å	1.844	1.849	1.842	1.837
Mn1−O3, Å	1.820	1.827	1.862	1.871
Mn2−O1, Å	1.891	1.902	1.912	1.917
Mn2−O2, Å	1.862	1.873	1.871	1.871
Mn2−O4, Å	1.866	1.883	1.825	1.836
Mn3−O1, Å	1.892	1.884	1.923	1.918
Mn3−O3, Å	1.830	1.826	1.829	1.834
Mn3−O4, Å	1.889	1.880	1.864	1.872
Ca1−O2, Å	2.452	2.515	2.391	2.489
Ca1−O3, Å	2.470	2.557	2.432	2.497
Ca1−O4, Å	2.660	2.603	2.430	2.490
Ca2−O4, Å	2.361	2.449		

[a]Compared by use of the dispersion-corrected TPSS functional.

Table 2. Exchange Coupling Constants as Fitted to Experimental Data[a] and to Calculated Values Based on Crystal Structures[b] and Geometry-Optimized Models[c]

model	J_{12} (cm^{-1})	J_{13} (cm^{-1})	J_{23} (cm^{-1})
$\mathbf{1}_{\mathrm{exp}}$	40.5	40.5	−10.8
$\mathbf{1}_{\mathrm{XRD}}$	27.0	36.3	−4.1
$\mathbf{1}_{\mathrm{opt}}$	26.6	36.1	−0.4
$\mathbf{2}_{\mathrm{XRD}}$	8.0	4.7	5.4
$\mathbf{2}_{\mathrm{opt}}$	7.2	7.0	7.0

[a]Structure $\mathbf{1}_{\mathrm{exp}}$. [b]Structures $\mathbf{1}_{\mathrm{XRD}}$ and $\mathbf{2}_{\mathrm{XRD}}$. [c]Structures $\mathbf{1}_{\mathrm{opt}}$ and $\mathbf{2}_{\mathrm{opt}}$.

dx.doi.org/10.1021/ja312552f | J. Am. Chem. Soc. 2013, 135, 5726−5739

the freely optimized model $\mathbf{2}_{opt}$. In view of the small magnitude of the computed coupling constants, it is probable that packing effects or choices in the fitting procedure may in practice result in a different distribution of J values than that predicted for the highly symmetric $\mathbf{2}_{opt}$.

For interpreting the nature of exchange coupling pathways, parallels can be drawn with simpler Mn complexes. Specifically, the cubane structure can be thought of as three fused Mn_2O_2 dimers: Mn1−Mn2 and Mn1−Mn3, which are bis-μ-oxo-μ-carboxylato-bridged, and Mn2−Mn3, which is bis-μ-oxo-bridged (Figure 3). From a recent study of Mn dimers,[42] it is known that a bis-μ-oxo-bridged Mn(IV) dimer without external constraints has Mn−O−Mn angles of 99° and a Mn−Mn distance of 2.82 Å. For the Mn2−Mn3 dimeric subunit of **1**, the distortion of these parameters from the ideal case is small, hence structural reasons are insufficient to interpret the quenching of antiferromagnetic exchange from −115 cm^{-1} in the ideal case to −4 cm^{-1} in the cubane subunit.

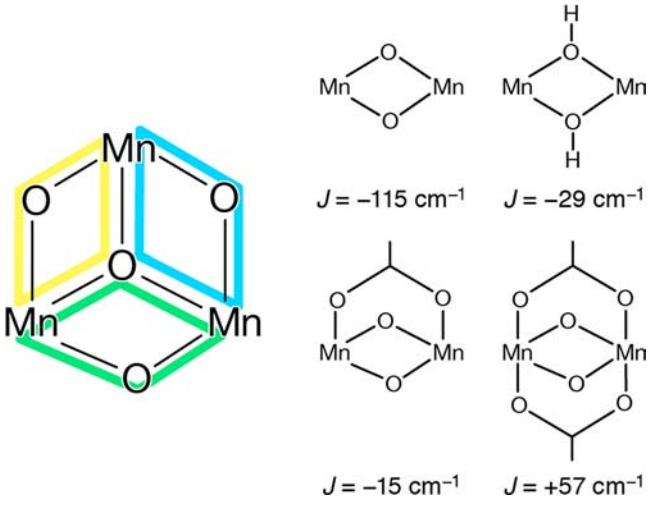

Figure 3. (Left) Notional decomposition of the Mn_3O_4 part of the cubanes into three fused Mn_2O_2 subunits. (Right) Representative bridging modes and exchange coupling constants of model Mn_2(IV,IV) dimers from ref 42.

A study of the effects of protonation of μ-oxo bridges on the exchange pathways in Mn dimers showed that protonation reduces the strength of the coupling.[42,90] For the protonated bis-μ-hydroxo-bridged Mn(IV) dimer, this yields a J value of −29 cm^{-1}.[42] Thus, a first explanation of the much weaker antiferromagnetic coupling in the Mn_2O_2 subunit of **1** can be suggested: Lewis acids at distances of 1.89 Å [Mn(IV)] and 2.66 and 2.36 Å (Ca^{2+}) interact with the oxo bridges with an effect similar to protonation, thus quenching the exchange pathways. The other two bis-μ-oxo-μ-carboxylato subunits of the cubane compare less favorably with the idealized bis-μ-oxo-μ-acetato case (J = −15 cm^{-1}), with the Mn−Mn distances and one of the Mn−O−Mn angles a little larger and the other Mn−O−Mn angle smaller. However, the small Mn−O−Mn angle is similar to that in the bis-μ-oxo-bis-μ-acetato dimer (J = +57 cm^{-1})[42] with *trans*-acetates. Constraints imposed by the remaining cubane atoms may be responsible for this similarity: the $MnCaO_2$ unit opposite the two Mn_2O_2 planes acts similarly to the second acetato bridge in the idealized system, forcing the Mn−O−Mn angles in the Mn1−Mn2 and Mn1−Mn3 dimeric subunits into the ferromagnetic coupling regime. As to why the magnitude of the coupling is smaller than in the dimer, two possible explanations are that the Mn−Mn distance in the idealized model is distinctly shorter (2.59 Å), and that Lewis acid interactions of the oxo bridges with Mn(IV) and Ca^{2+} diminish the exchange interactions for these subunits, in a way that mimics protonation effects.

The distances and angles of the dimeric subunits of **2** are closer to the ideal bis-μ-oxo-bridged case; it might have been expected that a hydroxo-bridged dimer would agree better, owing to the Lewis acid coordination analogy discussed above, but it is in fact more expanded in Mn−Mn/O distances and angles. Considering the steric effects of the remaining cubane atoms, the doubly protonated form of an ideal bis-μ-oxo-μ-carboxylato dimer presents the best match. However, the geometric parameters compare less favorably: the Mn−Mn distance is 0.25 Å longer and the Mn−OH−Mn angle is 4° wider, since structural relaxation in the dimer is not hindered by

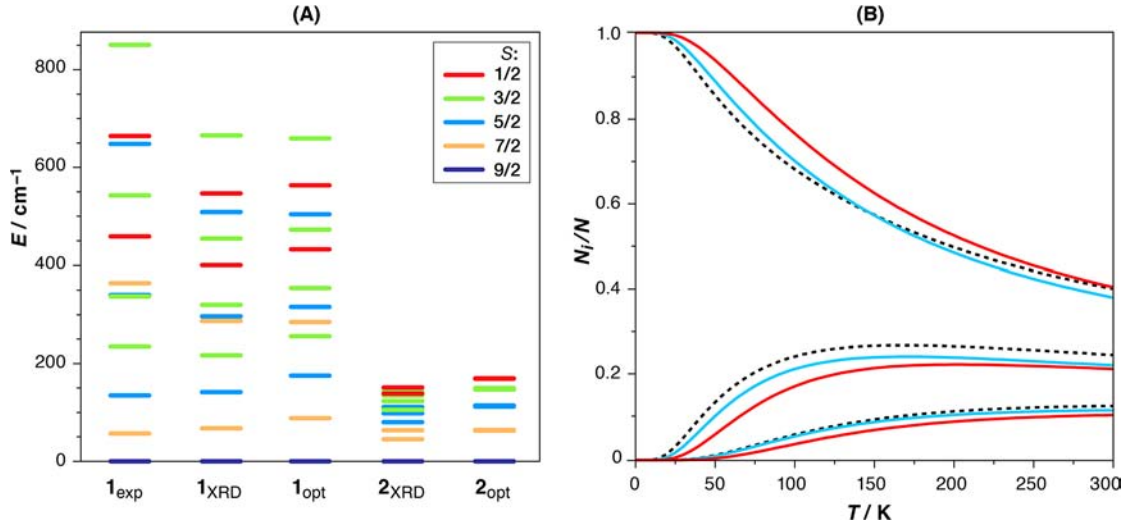

Figure 4. (A) Complete spin ladders based on experimentally fitted exchange coupling constants for **1** and computed values for XRD and optimized structures of **1** and **2**. (B) Boltzmann populations of the three lowest states of **1**, based on the Heisenberg spin ladder computed from the fitted J values (black dashed line) and on calculated values for XRD (blue line) and optimized (red line) structures.

dx.doi.org/10.1021/ja312552f | J. Am. Chem. Soc. 2013, 135, 5726−5739

additional constraints as in **2**. Despite this average structural agreement, the idealized bis-μ-oxo-μ-acetato-bridged dimer has J = +17 cm^{-1},[42] in line with the results for **2** of ca. 5−8 cm^{-1}.

Compared with the crystal structures, the ground states of the cubanes are stabilized upon geometry optimization. For **1**, this leads to more symmetric ferromagnetic interactions, but the strength of the antiferromagnetic pathway is more strongly underestimated in $\mathbf{1}_{opt}$. For both $\mathbf{1}_{XRD}$ and $\mathbf{1}_{opt}$, the ground state has $S = {}^9/_2$, in agreement with the fitted parameters ($\mathbf{1}_{exp}$ in Figure 4A).[33] As anticipated from the predominant ferromagnetic couplings, both **1** and **2** display $S = {}^9/_2$ ground states with $S = {}^7/_2$ first excited states. The energy difference between the ground and first excited state for $\mathbf{1}_{XRD}$ is 67.7 cm^{-1}, which compares well with the fitted value of 56.7 cm^{-1}. The above suggest a strong preference for high-spin configurations, a fact known for cubanelike Mn-oxo architectures in the field of single-molecule magnetism,[91] where, however, additional design considerations[92] come into play. An important aspect to notice for the spin ladder of the optimized complex **2** compared to the spin ladder based on the crystal structure is the clustering of nearly degenerate states of the same spin. Since $\mathbf{2}_{opt}$ is well approximated with an equilateral coupling scheme, this arises directly from the Hamiltonian of eq 4: with the small predicted J values, deviations of ∼2 cm^{-1} have a noticeable impact on the spin level spacing through the altered J/J' ratio.

To further compare the excited-state energetics, Figure 4B depicts the Boltzmann populations N_i/N of the three lowest levels for **1** (all levels for **1** and **2** are presented in Figure S1 in Supporting Information). The population dependence only on the relative magnitude of $J_{12/13}$ and J_{23} allows for a direct comparison of experimental and calculated data for **1**. As can be seen from the spin ladders in Figure 4, the three lowest states of $\mathbf{1}_{exp}$, $\mathbf{1}_{XRD}$, and $\mathbf{1}_{opt}$ are expected to be most relevant up to room temperature ($k_BT \approx 208$ cm^{-1} for T = 300 K). A very good agreement for the most populated states for all three pairs of exchange coupling constants is observed. The ground state becomes depopulated above 20 K, with concurrent population of the first excited state. The second excited state becomes populated above 50 K, while higher states participate significantly only above 80 K. The population of the first excited state plateaus at ca. 120 K. Higher states come into play with increasing temperature, but the ground state remains the most populated up to 300 K (40%). The same analysis for $\mathbf{2}_{XRD}$ (see Supporting Information) shows faster depopulation of the ground state than for **1**, reflecting the significantly smaller energy gaps between the ground and the lowest excited states for **2** (Figure 4A). As in **1**, the $S = {}^9/_2$ state remains the most highly populated up to 300 K.

A more direct way to compare experimental and calculated data is through the observable magnetic susceptibility. As seen in Figure 5, the agreement of simulated susceptibility for **1** with the $\mathbf{1}_{exp}$ fit is very good. For both sets of J values derived from $\mathbf{1}_{XRD}$ and $\mathbf{1}_{opt}$, the match is excellent up to ∼25 K. Between 25 and 180 K, the susceptibility based on $\mathbf{1}_{XRD}$ agrees better with experiment, whereas the curve based on $\mathbf{1}_{opt}$ is closer to $\mathbf{1}_{exp}$ for T > 210 K. This is due to the energetic separation of the first and second excited states from the ground state, which agrees better with the fitted values for data computed at the XRD structure. With $k_BT \approx 208$ cm^{-1} at 300 K, consideration of at least the first four states is required, complicating the interpretation of the better agreement of $\mathbf{1}_{opt}$ with $\mathbf{1}_{exp}$ at higher temperatures. Presumably the $\mathbf{1}_{XRD}$ curve diverges from

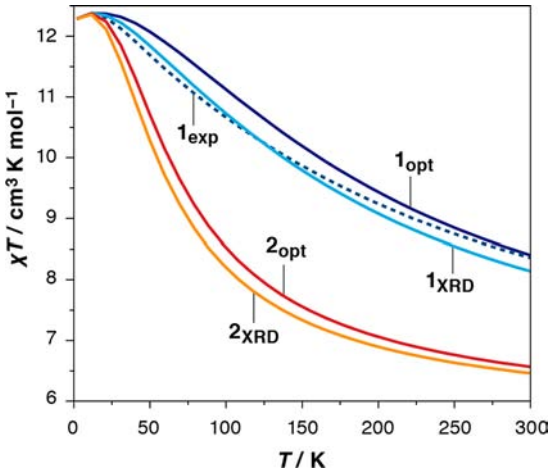

Figure 5. Plot of molar magnetic susceptibility χT vs T at **H** = 0.1 T based on the experimentally fitted J values for **1** and on the computed values for XRD and optimized structures of **1** and **2**.

$\mathbf{1}_{exp}$ because the third excited state is predicted to be too low in energy. The magnetic susceptibilities computed for $\mathbf{2}_{XRD}$ and $\mathbf{2}_{opt}$ are very similar. However, the general trend is different from that of **1**, showing a much more rapid change with temperature. This results from the faster population of excited states with increasing temperature: the whole spin ladder of **2** spans less than the thermal energy at 300 K, and hence all spin states contribute to the magnetic susceptibility at this temperature.

3.2. Differences between the Cubanes. By comparison of results for **1** and **2**, it is evident that **1** is adequately approximated by an isosceles spin coupling model but can be best described with three unequal exchange coupling interactions. Complex **2** shows instead weak ferromagnetic couplings between all centers, close to an approximately equilateral coupling scheme. Geometrically, the antiferromagnetically coupled Mn2−O2−Mn3 subunit of **1** is quite similar to the three subunits of **2**: the Mn−Mn and Mn−O distances are comparable, while the Mn−O−Mn angles in **1** (97.5° and 98.2° in the optimized structure) are within the range of the Mn−O−Mn angles of **2** (95°−100° for both $\mathbf{2}_{XRD}$ and $\mathbf{2}_{opt}$). However, the antiferromagnetic coupling minimum or possibly the switching point to ferromagnetic coupling is expected to lie in or close to this range, hence a switch in the sign of J should be easy. Beyond phenomenological structural parameters, factors that determine the position of this switching point are metal oxidation states and ligand electronic effects.[53] Although the oxidation states are the same, the ligand framework differs greatly between **1** and **2**.

A way to identify such effects is the analysis of exchange pathways. For dimers, such analysis is performed through the magnetic orbitals of the broken symmetry solution,[42,65,93,94] that is, the corresponding orbitals[95] that have an overlap significantly smaller than 1.[65] The magnitude of this overlap can be interpreted as the strength of the superexchange pathway. When the present cubanes are treated as trimers, no standard picture in terms of σ and π pathways can be obtained from any BS solution. Therefore, we used an atom substitution approach to "switch off" the pathways involving the third magnetic center for each Mn−Mn interaction by replacing each Mn(IV) with diamagnetic Ge^{4+}, which has a similar ionic radius. An analogous approach is used in the application of multireference

dx.doi.org/10.1021/ja312552f | J. Am. Chem. Soc. 2013, 135, 5726−5739

methods to oligonuclear systems.[48,96] The J values for the remaining spin sites are expected to be similar to those obtained from the complete spin Hamiltonian approach. This is true for **2**, but for **1** the antiferromagnetic pathway is lost even though no geometry relaxation was allowed (Table 3). This reflects the quantitative limitations of the pair decomposition approach.

Table 3. Exchange Coupling Constants and Overlaps of Magnetic Orbital Pairs in Ge^{4+}-Substituted Cubanes 1 and 2 for Each Mn Substitution Site

	complex **1**			complex **2**		
	Mn1	Mn2	Mn3	Mn1	Mn2	Mn3
J (cm^{-1})	15.6	35.2	24.2	14.1	13.9	14.0
pair 1	0.100	0.110	0.068	0.133	0.135	0.134
pair 2	0.051	0.050	0.057	0.038	0.037	0.038
pair 3	0.001	0.000	0.009	0.008	0.009	0.009

Nevertheless, three types of magnetic orbital pairs are now easily identified for **1** and **2**. The first contains two Mn d orbitals in the outside planes of the cubane that contain the Ca ion, with overlap at the O bridge connecting the Mn ions and Ca; the second comprises two Mn d orbitals in the face of the cubane parallel to the one containing the Ge and Ca ions, with overlap at the two O atoms in this plane; and the third contains the Mn d orbitals perpendicular to those of the first set of magnetic orbitals, with overlap at the O bridge connected to Mn and Ge ions only. Figure 6 shows a set of corresponding orbital pairs for cubane **2** (other sets are presented in Figure S2 in Supporting Information).

The order of these pairs in terms of overlap varies in general, but for most pathways the first described above is the most significant, with overlaps greater than 0.10 compared with less than 0.06 for other pathways. For **2**, the second and third type of pathway described above appear mixed and with minimal overlaps. The observed small-magnitude couplings are fully consistent with these small overlaps, particularly when contrasted with overlaps on the order of 0.25 that give rise to dominant superexchange interactions in antiferromagnetically coupled dimers.[42]

3.3. Hyperfine Coupling Constants. Isotropic hyperfine couplings of ^{55}Mn are listed in Table 4. The experimental values for **1** are given as site-specific isotropic HFCs obtained from a fit of ENDOR data with the isosceles coupling model, thus yielding equivalent parameters for Mn2 and Mn3. The differences in these values are small and fall within the range of known HFCs for Mn(IV) in natural and synthetic systems.[33,77,78,97−100] The computed HFCs for $\mathbf{1}_{XRD}$ deviate very little from those derived from the optimized geometry, and all have consistently smaller absolute values than the experimental values, which may arise from the scaling factor used.[46] Importantly, the differences between the calculated values for the three Mn ions are small for **1** and nonexistent for **2**, hence a unique manganese ion is not expected to be identifiable in a $Mn(IV)_3Ca$ cubane unless substantial asymmetry is imparted to the cluster by inequivalent coordination of supporting ligands. This is clearly not the case for the synthetic complexes studied in this work.

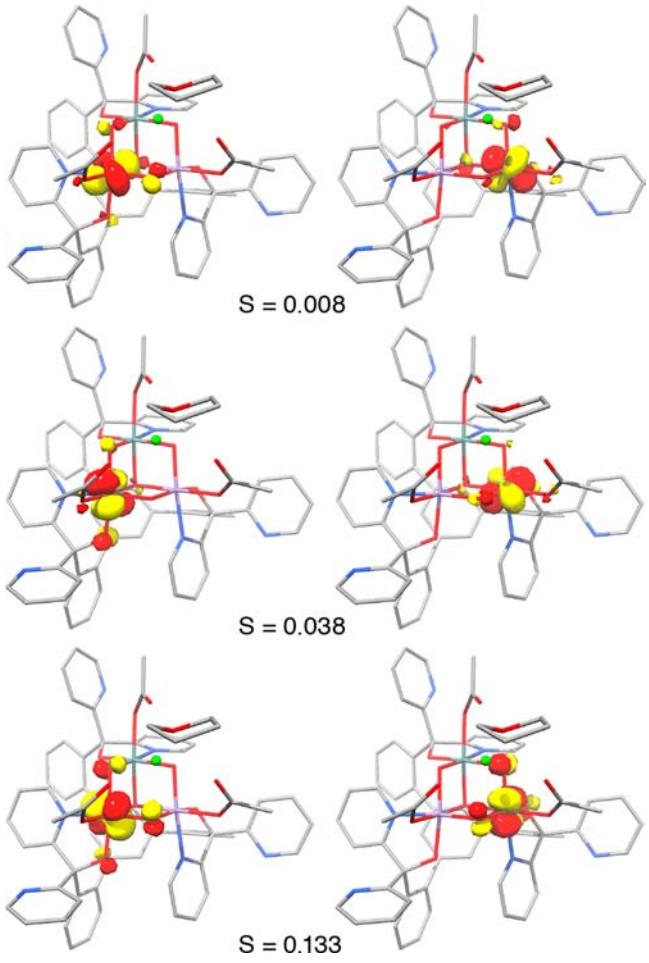

Figure 6. Corresponding orbital pairs and overlap integrals for **2** with Mn1 substituted by Ge^{4+}.

Table 4. Isotropic Effective ^{55}Mn Hyperfine Coupling Constants for Cubanes 1 and 2

	$A^{Mn1}_{iso,site}$ (MHz)	$A^{Mn2}_{iso,site}$ (MHz)	$A^{Mn3}_{iso,site}$ (MHz)
$\lvert\mathbf{1}_{exp}\rvert$	179	185	185
$\mathbf{1}_{XRD}$	−159	−166	−158
$\mathbf{1}_{opt}$	−161	−167	−159
$\mathbf{2}_{XRD}$	−147	−147	−147
$\mathbf{2}_{opt}$	−147	−147	−147

4. RESULTS ON IDEALIZED MODELS

The effects of oxo-bridge protonation and Mn reduction on the magnetic properties are highly relevant for the OEC and artificial catalysts, because they are intimately connected with the nature of catalytic sites and mechanistic steps.[2,101−103] Such effects can be studied more efficiently on smaller systems that model the synthetic cubanes. The models used for this purpose consist of a $Mn(IV)_3CaO_4$ core with acetates bridging all cubane faces except Mn2−Mn3, where the coordination sites are saturated with OH^- ligands to maintain some structural flexibility. An additional H_2O molecule was attached to Ca^{2+}, yielding the 50-atom model **3** (Figure 7).

4.1. Structures and Magnetism. The geometries of the idealized cubanes closely resemble the optimized structure of **1**. The largest difference is found for the Mn1−Mn3 distance (0.05 Å). Changes in Mn−Ca distances are more significant (−0.25 Å for Mn1−Ca), as a result of the less constrained Ca^{2+}

dx.doi.org/10.1021/ja312552f | J. Am. Chem. Soc. 2013, 135, 5726−5739

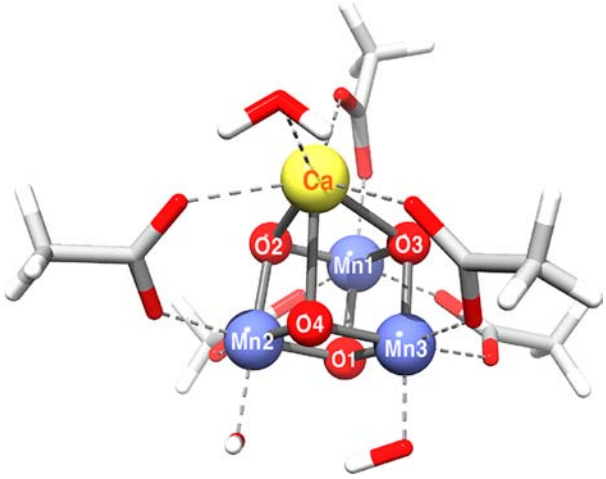

Figure 7. Structure of model complex **3**, with the labeling scheme for O and Mn centers.

coordination environment in the idealized models. Displacement of Ca^{2+} from the cluster leads to a Mn3−O3 elongation (1.92 Å). Although this is longer than usual for a Mn(IV)−μ-oxo bond, it does not perturb the spin populations (2.9−3.0 electrons for all Mn ions).

For **3**, three ferromagnetic pathways of similar magnitude (~20 cm^{-1}) are predicted. Inserting the frozen Mn_3CaO_4 core from the XRD structure of **1** into the ligand sphere of **3** (RMSD match of 0.030 Å for the Mn ions) leads to larger differences in the three J values (27.2, 26.5, and 20.8 cm^{-1} for J_{12}, J_{13}, and J_{23}, respectively). However, no antiferromagnetic interaction is observed. This is additional confirmation that the magnetic properties of a cubane are not uniquely determined by the core geometry but that the ligand environment exerts significant influence on the magnetic coupling. The idealized cubane has an $S = {}^9/_2$ ground state and an $S = {}^7/_2$ first excited state at 191 cm^{-1}, larger than the corresponding gap for **1** and **2**.

4.2. Oxo-bridge Protonation. Single protonation events of the oxo bridges of **3** lead to a distance increase of ~0.1 Å for the OH-bridged Mn−Mn pair. While all other Mn−Mn distances remain the same, OH-bridged Mn−Ca pairs expand more strongly (0.13−0.16 Å) than those that remain oxo-bridged (0.06−0.09 Å). The local impact of protonation is seen in Mn−O distances: Mn−OH bond lengths are up to 0.16 Å longer than the unprotonated Mn−O ones, while the oxo bridge of the same Mn_2O_2 subunit moves ~0.04 Å closer to the Mn ions. This is accompanied by a decrease of ~4.8° in the Mn−O−Mn angles, while the neighboring angle of the same subunit increases by ~5.7°. The same trends are observed for double and triple protonation, confirming that the geometric effects of single protonation events are largely independent of each other. The fully protonated **3**-H[1,2,3,4] (where protonation sites are indicated in brackets following the O atom labeling of Figure 7) is uniformly expanded relative to the parent compound.

Protonation of the tris-μ-oxo bridge (O1) is the energetically least favorable event. A similar observation was made in a study of models for a cobalt oxide water-oxidation catalyst.[104] Among the singly protonated isomers, the most stable is **3**-H[4], with **3**-H[2] and **3**-H[3] within 5 kcal·mol^{-1} (Table 5). Protonation of O1, however, requires 18.7 kcal·mol^{-1} relative to **3**-H[4]. The same trend of at least an additional 10 kcal·mol^{-1} required for O1 protonation is observed for the doubly and triply protonated isomers. Thus, O1 has the lowest proton affinity, while among the Ca^{2+}-bonding bridges O4 has the highest. Nonequivalent results are obtained for O2 and O3 protonation despite the very similar coordination environments, presumably as a result of the structural flexibility of the cubane. All fully relaxed models have an $S = {}^9/_2$ ground state and $S = {}^7/_2$ first excited state, regardless of the pattern and degree of protonation. Although one weakly antiferromagnetic pathway is observed in two cases, it does not inhibit the formation of a spin ${}^9/_2$ ground state.

Table 5. Relative Energies, J Couplings, and Energetic Separations between Ground and First Excited State for 3 and Its Fully Optimized Protonated Derivatives

model	E_{rel} (kcal·mol^{-1})	J_{12} (cm^{-1})	J_{13} (cm^{-1})	J_{23} (cm^{-1})	ΔE (cm^{-1})
3	0.0	22.0	20.7	23.2	191.2
3-H[1]	18.7	38.2	36.4	29.5	288.4
3-H[2]	4.5	7.4	16.6	18.3	96.6
3-H[3]	2.1	22.5	1.7	21.3	75.8
3-H[4]	0.0	20.9	19.6	6.9	102.1
3-H[1,2]	19.3	−3.1	20.1	12.7	27.8
3-H[1,3]	17.1	24.7	−0.4	28.8	76.9
3-H[1,4]	14.8	31.0	21.9	2.4	90.1
3-H[2,3]	6.7	16.9	8.4	16.3	99.9
3-H[2,4]	2.3	14.5	14.7	3.5	64.6
3-H[3,4]	0.0	18.8	12.8	9.5	99.0
3-H[1,2,3]	16.7	6.2	5.4	18.6	51.8
3-H[1,2,4]	12.6	6.0	11.0	6.7	57.1
3-H[1,3,4]	10.1	19.0	7.1	8.0	68.0
3-H[2,3,4]	0.0	14.3	11.3	1.6	47.0
3-H[1,2,3,4]	0.0	7.1	5.9	8.5	57.6

In an attempt to isolate the purely electronic effects of protonation, a second set of models was considered where only the proton positions were optimized and all other atoms were kept fixed at the geometry of **3**. Prohibiting structural relaxation (Table S4, Supporting Information) leads to two $S = {}^7/_2$ ground states (**3**-H[1,2] and **3**-H[1,3]), one $S = {}^5/_2$ ground state (**3**-H[1,2,4]) and two $S = {}^3/_2$ ground states (**3**-H[1,2,3] and **3**-H[1,2,3,4]), due to at least one pathway with $J \leq -8$ cm^{-1}, but an $S = {}^1/_2$ ground state is never observed. These results suggest at least two possibilities to form a ground state with total $S < {}^9/_2$: the presence of two antiferromagnetic couplings or of one single antiferromagnetic pathway comparable in magnitude to at least one of the ferromagnetic ones. The accessibility of specific spin states with respect to the ratios of exchange coupling constants will be further discussed below. At this point it is emphasized that the computed average structural relaxation energy per added proton exceeds 17 kcal·mol^{-1}. It seems improbable at this point that such high-energy geometric constraints permitting $S < {}^9/_2$ ground states could be realized in synthetic $Mn(IV)_3CaO_4$ cubane complexes.

Exchange couplings are generally weak for protonated cubanes across the whole series. **3**-H[1] exhibits the highest J values, all larger than in the parent compound. This can be attributed to the larger Mn−O−Mn angles for O2, O3, and O4, which are ~100° and thus of an order where ferromagnetic coupling is expected, compared with 95°−96° in **3** (full coordinates are given in the Supporting Information). The weakest coupling is observed for the fully protonated **3**-H[1,2,3,4], and the trends across the series support the

dx.doi.org/10.1021/ja312552f | J. Am. Chem. Soc. 2013, 135, 5726−5739

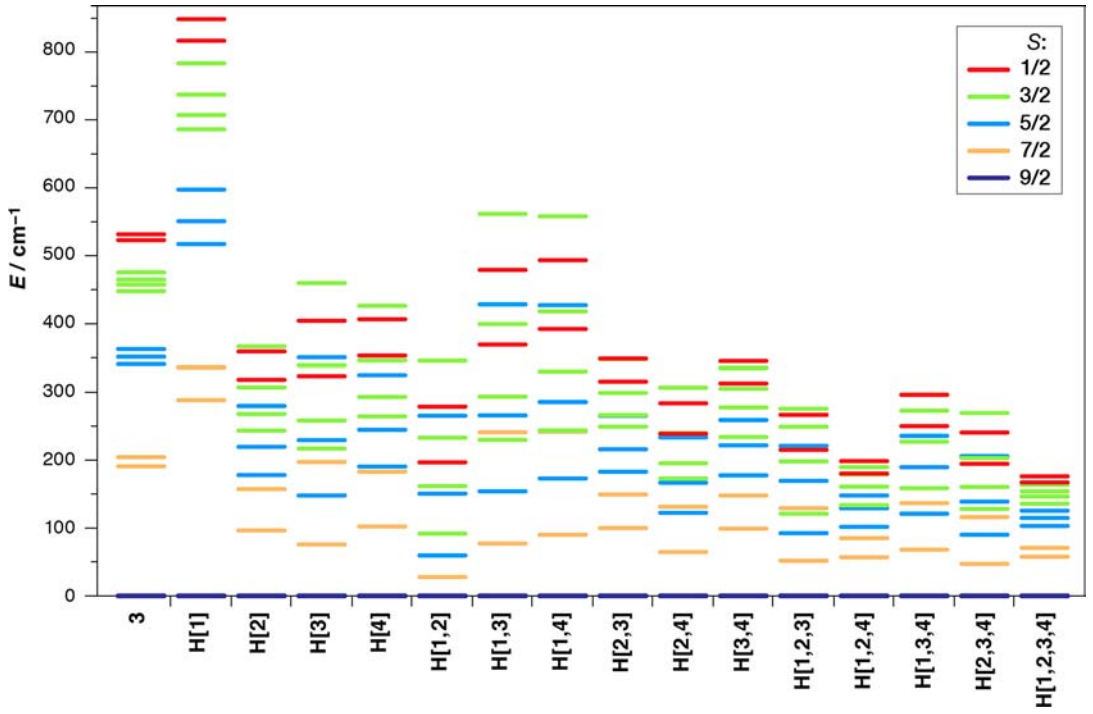

Figure 8. Spin ladders of cubane model **3** and all its possible protonation patterns up to fully protonated **3**-H[1,2,3,4]. Energies of excited states are given relative to the respective ground state of each fully optimized compound. All complexes have $S = {}^{9}/_{2}$ ground states.

decrease in exchange coupling strength upon increased protonation of the oxo bridges.[42,90] An important question is whether such single or multiple protonation events could be distinguished experimentally. The following results suggest that different degrees of protonation may be distinguishable for well-defined synthetic complexes. This is readily explained by the different spin ladders obtained for the four groups of compounds identified here (Figure 8).

While protonation of Ca^{2+}-bound oxo bridges results in ground−first excited state gaps of 75−102 cm^{-1}, protonation of the tris-μ-oxo-bridge O1 increases the gap to 288 cm^{-1}, well above the thermal energy at 300 K. For **3** it is expected that only the first and second excited states at 191 and 204 cm^{-1} are significantly populated at room temperature, since the third excited state is 340 cm^{-1} above the ground state. By contrast, the spin ladders of the triply protonated cubanes are significantly compressed compared to **3** or the singly protonated models, hence more states are populated up to room temperature. In fact, the average span of the spin ladder decreases linearly with the number of protons added to the cubane.

The above observations are reflected in the computed magnetic susceptibility. Single protonation of similar bridges, that is, O2, O3, or O4 versus O1, results in similar behavior; thus, the curves of **3**-H[2], **3**-H[3], and **3**-H[4] cluster together, well separated from that of **3** (Figure 9; see Figure S3 in Supporting Information for simulations for all models). On the other hand, the spin ladders of the more highly protonated cubanes, which have similar total energy span, lead to susceptibility curves characterized by a markedly steeper rate of change with T. Therefore, in combination with other data, these differences can be indicative of the extent of protonation in such cuboidal clusters.

4.3. Hyperfine Coupling Constants. For cubane **3**, the computed isotropic ^{55}Mn HFC values (Table S5, Supporting

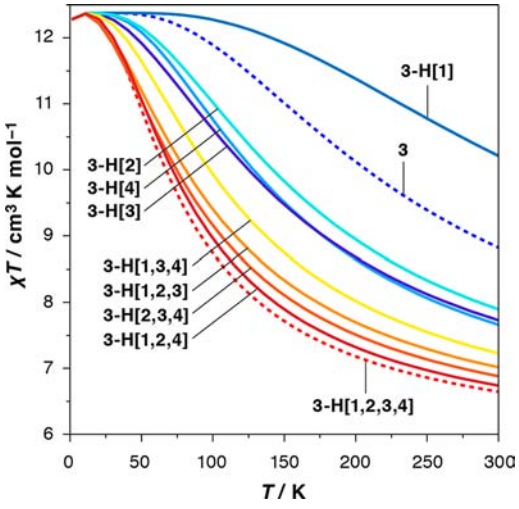

Figure 9. Plots of χT vs T for the singly and triply protonated derivates. Unprotonated cubane **3** and fully protonated cubane **3**-H[1,2,3,4] (dashed lines) are shown for reference.

Information) are larger in magnitude than for **1** and **2**, at −211 ± 1 MHz for all ions. The protonated complexes show smaller HFC values, in the range −156 to −203 MHz. Differences for centers with different coordination environments (Mn1 vs Mn2 and Mn3) can be related to geometric and electronic changes. However, the changes are rather subtle within a given protonated geometry, so differentiation would be difficult in practice. Mn centers coordinated by the hydroxo bridge in singly protonated models have HFC values of −180 to −190 MHz (Mn1) and −170 to −180 MHz (Mn2 and Mn3), whereas ions coordinated only by oxo bridges have HFC values of ca. −160 MHz. For the doubly protonated compounds, centers with one and two coordinated OH bridges are distinguishable owing to increased HFC values by ∼10 MHz,

dx.doi.org/10.1021/ja312552f | J. Am. Chem. Soc. 2013, 135, 5726−5739

but such differences may not be easily resolved experimentally. For triply protonated bridges the HFCs are again very similar, correlating with the elongation of Mn−O bonds that are not only local effects, as for single or double protonation, but influence the entire cubane geometry. With protonation-induced expansion of the system, the ^{55}Mn HFCs approach −200 MHz, closer to the values for **3**.

4.4. One-Center Reduction. Upon reduction of a Mn(IV) ion, its electronic configuration becomes high-spin d^4, which in near-octahedral environments leads to a Jahn−Teller (JT) distortion. Here this takes the form of a metal−ligand bond elongation of up to 0.3 Å, arising from occupation of an orbital of Mn d_{z^2} origin with metal−ligand σ-antibonding character. This is a signature of valence localization,[40,42] as confirmed by spin population analysis [~3.9 unpaired electrons for Mn(III) vs 2.9−3.0 electrons for Mn(IV) ions]. Ligands carry no spin density.

All Mn ions can be reduced in a $Mn(IV)_3Ca$ cubane, and each resulting Mn(III) has in principle three possible JT axis orientations. Although nine distinct minima can thus be envisioned, extensive searches with the unprotonated cubane **3** confirmed the existence of only one JT orientation for each Mn(III). These are along the axis that includes the tris-μ-oxo O1 for Mn1 and Mn2 (models **3**-R1 and **3**-R2) and along the axis that includes O4 for Mn3 (**3**-R3). Despite Mn−O bond elongations, all reduced models are of a "closed" cubane type, that is, the Mn ions remain effectively hexacoordinate; consequently, they are not directly comparable to the "open" form of the cubane that characterizes the OEC S_2-state core with the $S = {}^1/_2$ ground state, where a pentacoordinate Mn(III) is found. This point will be addressed in more detail in the Discussion.

3-R1 and **3**-R2 have a ferromagnetic ground state ($S = 5$), whereas the ground state of **3**-R3 is of intermediate spin, $S = 2$. To make an appropriate energetic comparison, the final single-point energy of the high-spin solution of **3**-R3 was lowered by the energetic stabilization of the projected ground state relative to the ninth excited state with $S = 5$ (362.6 cm^{-1}). **3**-R3 is the most stable reduced form, 4.8 and 1.8 $kcal \cdot mol^{-1}$ lower than **3**-R1 and **3**-R2, respectively. The ground state spin of **3**-R3 is connected to the antiferromagnetic Mn1−Mn3 pathway (Table 6). All other couplings are ferromagnetic and they increase

Table 6. Exchange Coupling Constants, Energetic Splitting between Ground and First Excited States, and Isotropic Effective ^{55}Mn Hyperfine Coupling Constants for $Mn(III)Mn(IV)_2CaO_4$ Cubanes

	J_{12} (cm^{-1})	J_{13} (cm^{-1})	J_{23} (cm^{-1})	ΔE (cm^{-1})	$A^{Mn1}_{iso,site}$ (MHz)	$A^{Mn2}_{iso,site}$ (MHz)	$A^{Mn3}_{iso,site}$ (MHz)
3-R1	42.1	40.3	6.5	203.8	−180	−142	−145
3-R2	8.7	9.2	48.9	89.3	−144	−231	−147
3-R3	20.5	−34.9	14.1	33.5	−147	−149	−166

significantly for at least one pathway involving the Mn(III) ion. Thus, the spin ladders also vary in span and in separation of the low-lying levels. The diversity of exchange coupling situations can be rationalized by considering that a JT distortion involving O1 has a different effect on the Mn−O−Mn angles than that involving a Ca^{2+}-bound oxo bridge. Although the same bridge is involved in the JT axes of **3**-R1 and **3**-R2, these are Mn ions with different coordination environments, thus leading to different coupling constants. The Mn(III) ion shows more negative HFC values than the Mn(IV) centers (−192 MHz on average), while the Mn(IV) centers in all models have values between −142 and −149 MHz, comparable in magnitude to those of **2** but smaller than for any of the protonated models derived from **3**.

5. DISCUSSION

The results presented in this work contribute toward a detailed profile of the properties of Mn_3CaO_4 cubanes. A crucial conclusion is that the $Mn(IV)_3CaO_4$ cubane is an intrinsically high-spin unit: all models considered herein exhibit an $S_T = {}^9/_2$ ground state. Although this is conclusive for the specific systems, it is worth considering the general conditions under which lower-spin ground states may arise. Figure 10 depicts maps of the ground state spin depending on the ratios of exchange coupling constants for the general case of three $S = {}^3/_2$ spin centers.

The total spin $S_T = {}^3/_2$ is dominant for most ratios of J values, while the maximum S_T of ${}^9/_2$ is also easily accessible for a wide range of J ratios. $S_T = {}^3/_2$ is exclusively the ground state with two negative and one positive J values, while when all J values are positive, only $S_T = {}^9/_2$ occurs. The lowest possible $S_T = {}^1/_2$ is achievable if *all three* exchange couplings are antiferromagnetic (see the spin ${}^1/_2$ "island" on the map of Figure 10b). Even when all exchange coupling constants are negative, however, introduction of significant asymmetry in the system (J ratios ≥ 3) still leads to the predominant $S_T = {}^3/_2$. The intermediate spins of ${}^5/_2$ and ${}^7/_2$ are accessible as ground states only for very narrow ranges of J ratios. The lower left quadrant of Figure 10b is of special interest in this respect and in relation to **1** as it shows how strong the unique negative J_{23} should be with respect to the positive ones in order to access $S_T \neq {}^9/_2$. Thus, $S_T = {}^7/_2$ can become the ground state if the antiferromagnetic pathway is at least half as strong as the ferromagnetic ones, while if they become equal in strength then even $S_T = {}^5/_2$ can become the ground state within a limited range of J ratios. Could these situations be realized in a cubane framework? The results presented in this paper do not strictly exclude this possibility but point to a negative answer.

An example of an $S_T = {}^1/_2$ trinuclear Mn(IV) system has been recently described by Baffert et al.[47] The $[Mn_3O_4(terpy)(terpyO_2)_2(H_2O)](S_2O_8)_2$ complex (Figure S5, Supporting Information) contains a triangular $Mn(IV)_3O_4$ core built of a bis-μ-oxo Mn_2O_2 unit where each Mn ion is linked to the third Mn ion via mono-μ-oxo bridges. This topology enables fairly strong antiferromagnetic interactions of similar magnitude between all ion pairs: consistent with the spin maps discussed here, variable-temperature magnetic susceptibility data and calculations of the same type as those employed in the present work indicate the presence of two equivalent pathways involving the mono-μ-oxo ion pairs ($J_{exp} = -37$ cm^{-1}, $J_{DFT} = -39$ cm^{-1}) and a distinct pathway for the bis-μ-oxo unit ($J_{exp} = -53$ cm^{-1}, $J_{DFT} = -56$ cm^{-1}).[47] This type of core topology is typically associated with $S_T = {}^1/_2$ ground states,[105,106] or more rarely with an $S_T = {}^3/_2$ ground state when, as shown on the spin maps, the J ratios fall outside the limited $S_T = {}^1/_2$ region.[107] As such, this more loosely connected core lies in the opposite side of the magnetic interaction spectrum compared to the structurally restrained cubanes studied in the present work, whose acute Mn−O−Mn angles hamper superexchange.

In view of the above, the chemical implausibility (a combination of site inequivalence and ligand flexibility) of establishing three $J < 0$ pathways of similar magnitude in an

dx.doi.org/10.1021/ja312552f | J. Am. Chem. Soc. 2013, 135, 5726−5739

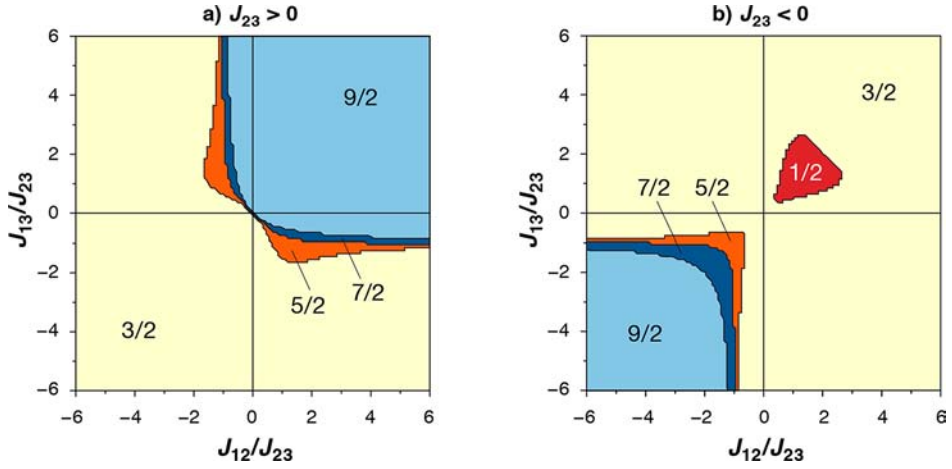

Figure 10. Maps indicating dependence of total spin of the ground state on ratios of exchange coupling constants for systems of three coupled $S = {}^3/_2$ spin sites, such as the $Mn(IV)_3CaO_4$ cubanes, for (a) positive and (b) negative reference J constant.

oxo-bridged $Mn(IV)_3CaO_4$ cubane excludes access to an $S_T = {}^1/_2$ ground state. At the same time, the high symmetry leads to magnetic couplings of similar magnitude; this is precisely what happens in **2**, which falls in the upper right quadrant of Figure 10a. **1** falls within the other ${}^9/_2$ region (lower left quadrant of Figure 10b) because two conditions are fulfilled: (i) the $J < 0$ coupling is significantly weaker than the two $J > 0$ ones and (ii) the $J > 0$ pathways are of similar strength, so the system is not drawn sufficiently away from the map diagonal toward regions of lower spin.

To examine the relevance of the present $Mn(IV)_3CaO_4$ cubanes to the OEC, we note that the first state of the Kok cycle with three Mn(IV) ions is S_2 (III, IV, IV, IV), which follows the one-electron oxidation of S_1 (III, III, IV, IV). Therefore, S_2 is also the first state of the OEC where a $Mn(IV)_3CaO_4$ cubane unit may arise; recent studies of structure–property correlations for the OEC suggest that indeed it does. Specifically, the core of the OEC in the S_2 state was shown to exist in two quasi-isoenergetic structural forms that are interconvertible over a low barrier (Figure 11).[15] These two forms are valence isomers in which the unique Mn(III) is found in either of the two terminal positions; combined with the rearrangements that follow this valence exchange, different magnetic couplings, spin states, and spectroscopic signatures result for each form.

The first form ($S_T = {}^1/_2$, $g \sim 2.0$) is similar to a model advanced by Siegbahn[108−110] and resembles in connectivity a model proposed by analysis of polarized EXAFS data,[76,111,112] while the second form ($S_T = {}^5/_2$, $g \geq 4.1$) resembles a model described by Barber and Murray.[113] Crucial for our considerations is the presence of a distinct $Mn(IV)_3CaO_4$ cubane subunit in the $S_T = {}^5/_2$ form of the OEC. The exchange couplings within this Mn(IV) trimer part are all ferromagnetic and within the ranges observed for the cubane systems studied here. Unsurprisingly, the J values for the cubane alone lead to an $S = {}^9/_2$ spin state for this subunit of the OEC, in perfect analogy with all $Mn(IV)_3CaO_4$ cubanes. It is the antiferromagnetic coupling of this high-spin subunit with the "dangling" Mn(III) ion that lowers the total spin of this form, leading to $S_T = {}^5/_2$. It is noted that the ^{55}Mn HFC values obtained for cubanes **1**, **2**, and **3** are all within the range of calculated isotropic on-site HFCs for Mn(IV) in the $S_T = {}^5/_2$ model of the OEC (146–160 MHz).[15]

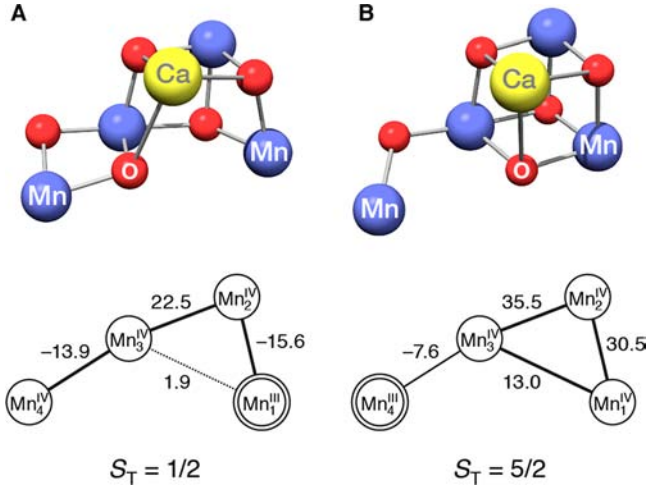

Figure 11. Two structural forms of the inorganic core of the OEC in the S_2 state (coordinating ligands not shown). (A) The first form has an $S_T = {}^1/_2$ ground state and corresponds to the $g \sim 2.0$ multiline EPR signal of the OEC. (B) The second form has an $S_T = {}^5/_2$ ground state and corresponds to the $g \geq 4.1$ signals; it is the form that contains a $Mn(IV)_3CaO_4$ ($S = {}^9/_2$) subunit.

An older proposal for the OEC structure, based on the XRD model of Ferreira et al.,[114] consisted of a Mn_3CaO_4 cubane with a dangling Mn ion attached directly to one of the cubane oxo bridges. Since this arrangement does not enable large antiferromagnetic couplings between the outer and the cubane ions, such a structure cannot produce a spectroscopically consistent model for any of the observable S_2-state EPR signals. This seems to have been overlooked in part of the literature[115−117] before the most recent advances in the crystallography of PS-II.[10]

The $S_T = {}^1/_2$ form of the OEC that gives rise to the characteristic $g \sim 2.0$ multiline EPR spectrum of PS-II in the S_2 state is obtained by "opening" the cubane of the $S_T = {}^5/_2$ form. This valence rearrangement, an effective one-electron reduction of the $Mn(IV)_3Ca$ cubane subunit by the external Mn(III) ion, is followed by structural changes that drastically modify the magnetic couplings: J_{13} is diminished while J_{12} changes sign as the Mn1−O−Mn2 angle widens considerably. Thus, by reference to the OEC, it is more understandable why no genuinely pentacoordinate Mn(III) ion and no Mn−O bond

dx.doi.org/10.1021/ja312552f | J. Am. Chem. Soc. 2013, 135, 5726−5739

breaking were observed in the reduced models of **3**: in the OEC, the interconversion is facilitated by the external Mn ion. In agreement with the energetic proximity of the two S_2-state conformations, the opening of the cubane involves a simple bond rearrangement and not a change in the total number and kind of bonds. This is potentially critical for reactivity, since the flexible oxo is probably one of the substrates for O−O bond formation.[3,118]

The results obtained for the one-electron reduction of **3** suggest that, for each Mn(III), one specific Jahn−Teller axis orientation is preferred. This is precisely what is observed in the OEC. Different proposals have been advanced regarding the JT axis orientation for Mn1 in the III oxidation state, specifically, alignment with either His332[119] or Asp342.[108] Current models indicate that only the second option is realizable, while both Mn centers that can be Mn(III) in the S_2 state (Mn1 and Mn4 in Figure 11) are characterized by only one possible JT orientation.[15,76]

It is interesting to consider whether this cubane opening described above, and shown to be so intimately connected with the observable properties and potentially with the catalytic function of the OEC, is also relevant to the Mn/Ca birnessite-like oxides. Siegbahn[108−110] has described a water oxidation mechanism for the OEC that involves substrate water binding during the S_2−S_3 transition to the open coordination site of Mn(III) (Figure 11, left). If such a mechanism is assumed to be general, it implies that the $Mn(IV)_3CaO_4$ cubane subunit, if present in a catalytic system (Figure 11, right), would have to open up and form an available site for substrate binding.

As discussed above, in the OEC the prerequisite for this is effective intramolecular reduction of the $Mn(IV)_3CaO_4$ subunit by a proximal Mn(III) ion and concomitant Mn−O bond rearrangement. We presume that this can equally well be realized in the Mn/Ca oxide catalysts because of the availability of neighboring Mn ions in the lattice that can participate in electron exchange. Since, however, this hypothetical process is not yet fully connected with experimental observables, it is not possible to confirm its role in the actual water oxidation mechanism(s). Accordingly, the mechanistic role of Ca cannot be clarified with confidence at this stage, although if such a cubane-opening process is functionally relevant, then a possible role for Ca would be to dictate the orientation of the electron-transfer process and hence to direct substrate binding. This issue will be more adequately addressed in a forthcoming study of Mn/Ca oxides.

6. CONCLUSIONS

The $Mn(IV)_3CaO_4$ complexes reported by the groups of Agapie[32] and Christou[33] offer a unique opportunity to study the electronic structure and magnetic properties of systems that resemble the OEC and synthetic Mn/Ca water oxidizing catalysts but are much easier to characterize and understand. Our study confirms that these systems have a spin $^9/_2$ ground state, which emerges as an intrinsic property of the cubanes. Geometric considerations are not sufficient to reliably deduce the signs and relative magnitudes of magnetic couplings, since the ligand environment exerts a significant influence. However, even if one antiferromagnetic pathway arises in a cubane framework, a low-spin ground state is inaccessible. Therefore, the presence of a $Mn(IV)_3CaO_4$ cubane is associated with the presence of an $S = {}^9/_2$ subunit; conversely, a total spin incompatible with such a high-spin subunit reveals the absence of an intact $Mn(IV)_3CaO_4$ cubane.

Comparison with the S_2 state of the OEC shows that complexes **1** and **2** are highly relevant to the $S_T = {}^5/_2$ form that gives rise to the $g \geq 4.1$ EPR signals. However, they are not models for the low-spin $S_T = {}^1/_2$ form that gives rise to the multiline $g \sim 2$ signal, nor are they expected to become so by simple one-electron reduction. A reduction-induced opening of the cubane as in the OEC, leading to an open coordination site that may be implicated in water substrate binding, apparently requires an alternative external bonding partner. Since this requirement is fulfilled in both natural and artificial catalysts, it is likely that such a structural process is a feature of both. It remains to be examined whether it is also a common feature of the catalytic mechanism.

■ ASSOCIATED CONTENT

Supporting Information

Additional computational details and discussion; six tables and five figures as discussed in the text; and total energies and Cartesian coordinates of all optimized structures. This material is available free of charge via the Internet at http://pubs.acs.org.

■ AUTHOR INFORMATION

Corresponding Author

dimitrios.pantazis@cec.mpg.de.

Notes

The authors declare no competing financial interest.

■ ACKNOWLEDGMENTS

We thank Dr. Eckhard Bill for discussions on magnetic susceptibility simulations. Financial support was provided by the Max Planck Society.

■ REFERENCES

(1) McEvoy, J. P.; Brudvig, G. W. *Chem. Rev.* **2006**, *106*, 4455.
(2) Messinger, J.; Renger, G. In *Primary Processes of Photosynthesis, Part 2: Principles and Apparatus*; The Royal Society of Chemistry: Cambridge, U.K., 2008; Vol. 9, p 291.
(3) Cox, N.; Pantazis, D. A.; Neese, F.; Lubitz, W. *Acc. Chem. Res.* **2013**, DOI: 10.1021/ar3003249.
(4) Lubitz, W.; Reijerse, E. J.; Messinger, J. *Energy Environ. Sci.* **2008**, *1*, 15.
(5) Dau, H.; Limberg, C.; Reier, T.; Risch, M.; Roggan, S.; Strasser, P. *ChemCatChem* **2010**, *2*, 724.
(6) Najafpour, M. M.; Govindjee. *Dalton Trans.* **2011**, *40*, 9076.
(7) Najafpour, M. M.; Moghaddam, A. N.; Allakhverdiev, S. I.; Govindjee. *Biochim. Biophys. Acta Bioenerg.* **2012**, *1817*, 1110.
(8) Kok, B.; Forbush, B.; McGloin, M. *Photochem. Photobiol.* **1970**, *11*, 457.
(9) Ghanotakis, D. F.; Babcock, G. T.; Yocum, C. F. *FEBS Lett.* **1984**, *167*, 127.
(10) Umena, Y.; Kawakami, K.; Shen, J.-R.; Kamiya, N. *Nature* **2011**, *473*, 55.
(11) Luber, S.; Rivalta, I.; Umena, Y.; Kawakami, K.; Shen, J. R.; Kamiya, N.; Brudvig, G. W.; Batista, V. S. *Biochemistry* **2011**, *50*, 6308.
(12) Grundmeier, A.; Dau, H. *Biochim. Biophys. Acta, Bioenerg.* **2012**, *1817*, 88.
(13) Galstyan, A.; Robertazzi, A.; Knapp, E. W. *J. Am. Chem. Soc.* **2012**, *134*, 7442.
(14) Yamaguchi, K.; Isobe, H.; Yamanaka, S.; Saito, T.; Kanda, K.; Shoji, M.; Umena, Y.; Kawakami, K.; Shen, J. R.; Kamiya, N.; Okumura, M. *Int. J. Quantum Chem.* **2012**, *113*, 525.
(15) Pantazis, D. A.; Ames, W.; Cox, N.; Lubitz, W.; Neese, F. *Angew. Chem., Int. Ed.* **2012**, *51*, 9935.
(16) Wiechen, M.; Berends, H.-M.; Kurz, P. *Dalton Trans.* **2012**, *41*, 21.

(17) Najafpour, M. M.; Pashaei, B.; Nayeri, S. *Dalton Trans.* **2012**, *41*, 4799.
(18) Najafpour, M. M.; Ehrenberg, T.; Wiechen, M.; Kurz, P. *Angew. Chem., Int. Ed.* **2010**, *49*, 2233.
(19) Zaharieva, I.; Najafpour, M. M.; Wiechen, M.; Haumann, M.; Kurz, P.; Dau, H. *Energy Environ. Sci.* **2011**, *4*, 2400.
(20) Hocking, R. K.; Brimblecombe, R.; Chang, L.-Y.; Singh, A.; Cheah, M. H.; Glover, C.; Casey, W. H.; Spiccia, L. *Nat. Chem.* **2011**, *3*, 461.
(21) Pecoraro, V. L.; Baldwin, M. J.; Caudle, M. T.; Hsieh, W.-Y.; Law, N. A. *Pure Appl. Chem.* **1998**, *70*, 925.
(22) Limburg, J.; A. Szalai, V.; W. Brudvig, G. *J. Chem. Soc., Dalton Trans.* **1999**, 1353.
(23) Zheng, M.; Dismukes, G. C. *Inorg. Chem.* **1996**, *35*, 3307.
(24) Jaszewski, A. R.; Petrie, S.; Pace, R. J.; Stranger, R. *Chem.—Eur. J.* **2011**, *17*, 5699.
(25) Pace, R. J.; Jin, L.; Stranger, R. *Dalton Trans.* **2012**, *41*, 11145.
(26) Messinger, J.; Robblee, J. H.; Bergmann, U.; Fernandez, C.; Glatzel, P.; Visser, H.; Cinco, R. M.; McFarlane, K. L.; Bellacchio, E.; Pizarro, S. A.; Cramer, S. P.; Sauer, K.; Klein, M. P.; Yachandra, V. K. *J. Am. Chem. Soc.* **2001**, *123*, 7804.
(27) Mishra, A.; Wernsdorfer, W.; Abboud, K. A.; Christou, G. *Chem. Commun.* **2005**, 54.
(28) Hewitt, I. J.; Tang, J.-K.; Madhu, N. T.; Clerac, R.; Buth, G.; Anson, C. E.; Powell, A. K. *Chem. Commun.* **2006**, 2650.
(29) Kotzabasaki, V.; Siczek, M.; Lis, T.; Milios, C. J. *Inorg. Chem. Commun.* **2011**, *14*, 213.
(30) Nayak, S.; Nayek, H. P.; Dehnen, S.; Powell, A. K.; Reedijk, J. *Dalton Trans.* **2011**, *40*, 2699.
(31) Park, Y. J.; Ziller, J. W.; Borovik, A. S. *J. Am. Chem. Soc.* **2011**, *133*, 9258.
(32) Kanady, J. S.; Tsui, E. Y.; Day, M. W.; Agapie, T. *Science* **2011**, *333*, 733.
(33) Mukherjee, S.; Stull, J. A.; Yano, J.; Stamatatos, T. C.; Pringouri, K.; Stich, T. A.; Abboud, K. A.; Britt, R. D.; Yachandra, V. K.; Christou, G. *Proc. Natl. Acad. Sci. U.S.A.* **2012**, *109*, 2257.
(34) McGrady, J. E.; Stranger, R. *J. Am. Chem. Soc.* **1997**, *119*, 8512.
(35) Zhao, X. G.; Richardson, W. H.; Chen, J. L.; Li, J.; Noodleman, L.; Tsai, H. L.; Hendrickson, D. N. *Inorg. Chem.* **1997**, *36*, 1198.
(36) Delfs, C. D.; Stranger, R. *Inorg. Chem.* **2001**, *40*, 3061.
(37) Barone, V.; Bencini, A.; Gatteschi, D.; Totti, F. *Chem.—Eur. J.* **2002**, *8*, 5019.
(38) Petrie, S.; Mukhopadhyay, S.; Armstrong, W. H.; Stranger, R. *Phys. Chem. Chem. Phys.* **2004**, *6*, 4871.
(39) Rudberg, E.; Sałek, P.; Rinkevicius, Z.; Ågren, H. *J. Chem. Theory Comput.* **2006**, *2*, 981.
(40) Orio, M.; Pantazis, D. A.; Petrenko, T.; Neese, F. *Inorg. Chem.* **2009**, *48*, 7251.
(41) Schinzel, S.; Kaupp, M. *Can. J. Chem.* **2009**, *87*, 1521.
(42) Pantazis, D. A.; Krewald, V.; Orio, M.; Neese, F. *Dalton Trans.* **2010**, *39*, 4959.
(43) Schraut, J.; Arbuznikov, A. V.; Schinzel, S.; Kaupp, M. *ChemPhysChem* **2011**, *12*, 3170.
(44) Bovi, D.; Guidoni, L. *J. Chem. Phys.* **2012**, *137*, No. 114107.
(45) Isobe, H.; Shoji, M.; Koizumi, K.; Kitagawa, Y.; Yamanaka, S.; Kuramitsu, S.; Yamaguchi, K. *Polyhedron* **2005**, *24*, 2767.
(46) Pantazis, D. A.; Orio, M.; Petrenko, T.; Zein, S.; Bill, E.; Lubitz, W.; Messinger, J.; Neese, F. *Chem.—Eur. J.* **2009**, *15*, 5108.
(47) Baffert, C.; Orio, M.; Pantazis, D. A.; Duboc, C.; Blackman, A. G.; Blondin, G.; Neese, F.; Deronzier, A.; Collomb, M.-N. *Inorg. Chem.* **2009**, *48*, 10281.
(48) Fliegl, H.; Fink, K.; Klopper, W.; Anson, C. E.; Powell, A. K.; Clerac, R. *Phys. Chem. Chem. Phys.* **2009**, *11*, 3900.
(49) Pantazis, D. A.; Orio, M.; Petrenko, T.; Zein, S.; Lubitz, W.; Messinger, J.; Neese, F. *Phys. Chem. Chem. Phys.* **2009**, *11*, 6788.
(50) Schinzel, S.; Schraut, J.; Arbuznikov, A. V.; Siegbahn, P. E. M.; Kaupp, M. *Chem.—Eur. J.* **2010**, *16*, 10424.
(51) Kanda, K.; Yamanaka, S.; Saito, T.; Kawakami, T.; Kitagawa, Y.; Okumura, M.; Nakamura, H.; Yamaguchi, K. *Polyhedron* **2011**, *30*, 3256.
(52) Bencini, A.; Gatteschi, D. *EPR of Exchange Coupled Systems*; Springer Verlag: Berlin, 1990; p 287.
(53) Kahn, O. *Molecular Magnetism*; VCH: New York, 1993; p 396.
(54) Bastardis, R.; Guihery, N.; de Graaf, C. *J. Chem. Phys.* **2008**, *129*, No. 104102.
(55) Kambe, K. *J. Phys. Soc. Jpn.* **1950**, *5*, 48.
(56) Parr, R. G.; Yang, W. *Density-Functional Theory of Atoms and Molecules*; Oxford University Press: Oxford, U.K., 1989; p 352.
(57) Ginsberg, A. P. *J. Am. Chem. Soc.* **1980**, *102*, 111.
(58) Noodleman, L. *J. Chem. Phys.* **1981**, *74*, 5737.
(59) Noodleman, L.; Davidson, E. R. *Chem. Phys.* **1986**, *109*, 131.
(60) Yamaguchi, K.; Takahara, Y.; Fueno, T. In *Applied Quantum Chemistry*; Smith V. H., Jr., Scheafer, H. F., III, Morokuma, K., Eds.; D. Reidel: Boston, 1986; p 155.
(61) Yamaguchi, K.; Tsunekawa, T.; Toyoda, Y.; Fueno, T. *Chem. Phys. Lett.* **1988**, *143*, 371.
(62) Yamanaka, S.; Kawakami, T.; Nagao, H.; Yamaguchi, K. *Chem. Phys. Lett.* **1994**, *231*, 25.
(63) Caballol, R.; Castell, O.; Illas, F.; Moreira, I. d. P. R.; Malrieu, J. P. *J. Phys. Chem. A* **1997**, *101*, 7860.
(64) Bencini, A.; Totti, F.; Daul, C. A.; Doclo, K.; Fantucci, P.; Barone, V. *Inorg. Chem.* **1997**, *36*, 5022.
(65) Neese, F. *J. Phys. Chem. Solids* **2004**, *65*, 781.
(66) Ruiz, E. *Struct. Bonding (Berlin)* **2004**, *113*, 91.
(67) Neese, F. *J. Biol. Inorg. Chem.* **2006**, *11*, 702.
(68) Shoji, M.; Koizumi, K.; Kitagawa, Y.; Kawakami, T.; Yamanaka, S.; Okumura, M.; Yamaguchi, K. *Chem. Phys. Lett.* **2006**, *432*, 343.
(69) Moreira, I. d. P. R.; Illas, F. *Phys. Chem. Chem. Phys.* **2006**, *8*, 1645.
(70) Orio, M.; Pantazis, D. A.; Neese, F. *Photosynth. Res.* **2009**, *102*, 443.
(71) Bencini, A.; Totti, F. *J. Chem. Theory Comput.* **2009**, *5*, 144.
(72) Neese, F. *Coord. Chem. Rev.* **2009**, *253*, 526.
(73) Neese, F.; Ames, W.; Christian, G.; Kampa, M.; Liakos, D. G.; Pantazis, D. A.; Roemelt, M.; Surawatanawong, P.; Ye, S. F. *Adv. Inorg. Chem.* **2010**, *62*, 301.
(74) Sproviero, E. M.; Gascon, J. A.; McEvoy, J. P.; Brudvig, G. W.; Batista, V. S. *J. Inorg. Biochem.* **2006**, *100*, 786.
(75) O'Brien, T. A.; Davidson, E. R. *Int. J. Quantum Chem.* **2003**, *92*, 294.
(76) Ames, W.; Pantazis, D. A.; Krewald, V.; Cox, N.; Messinger, J.; Lubitz, W.; Neese, F. *J. Am. Chem. Soc.* **2011**, *133*, 19743.
(77) Cox, N.; Rapatskiy, L.; Su, J.-H.; Pantazis, D. A.; Sugiura, M.; Kulik, L.; Dorlet, P.; Rutherford, A. W.; Neese, F.; Boussac, A.; Lubitz, W.; Messinger, J. *J. Am. Chem. Soc.* **2011**, *133*, 3635.
(78) Su, J.-H.; Cox, N.; Ames, W.; Pantazis, D. A.; Rapatskiy, L.; Lohmiller, T.; Kulik, L. V.; Dorlet, P.; Rutherford, A. W.; Neese, F.; Boussac, A.; Lubitz, W.; Messinger, J. *Biochim. Biophys. Acta, Bioenerg.* **2011**, *1807*, 829.
(79) Tao, J.; Perdew, J. P.; Staroverov, V. N.; Scuseria, G. E. *Phys. Rev. Lett.* **2003**, *91*, No. 146401.
(80) Staroverov, V. N.; Scuseria, G. E.; Tao, J.; Perdew, J. P. *J. Chem. Phys.* **2003**, *119*, 12129.
(81) van Lenthe, E.; Baerends, E. J.; Snijders, J. G. *J. Chem. Phys.* **1994**, *101*, 9783.
(82) van Lenthe, E.; Snijders, J. G.; Baerends, E. J. *J. Chem. Phys.* **1996**, *105*, 6505.
(83) Pantazis, D. A.; Chen, X. Y.; Landis, C. R.; Neese, F. *J. Chem. Theory Comput.* **2008**, *4*, 908.
(84) Schäfer, A.; Huber, C.; Ahlrichs, R. *J. Chem. Phys.* **1994**, *100*, 5829.
(85) Neese, F.; Wennmohs, F.; Hansen, A.; Becker, U. *Chem. Phys.* **2009**, *356*, 98.
(86) Neese, F. *Wiley Interdiscip. Rev.: Comput. Mol. Sci.* **2012**, *2*, 73.
(87) Grimme, S.; Antony, J.; Ehrlich, S.; Krieg, H. *J. Chem. Phys.* **2010**, *132*, No. 154104.

(88) Klamt, A.; Schüürman, D. *J. Chem. Soc., Perkin Trans. 2* **1993**, 799.
(89) Bill, E. *JulX program*; Max Planck Institute for Bioinorganic Chemistry, Mülheim an der Ruhr, Germany, 2008.
(90) Baldwin, M. J.; Stemmler, T. L.; Riggs-Gelasco, P. J.; Kirk, M. L.; Penner-Hahn, J. E.; Pecoraro, V. L. *J. Am. Chem. Soc.* **1994**, *116*, 11349.
(91) Inglis, R.; Stoumpos, C. C.; Prescimone, A.; Siczek, M.; Lis, T.; Wernsdorfer, W.; Brechin, E. K.; Milios, C. J. *Dalton Trans.* **2010**, *39*, 4777.
(92) Neese, F.; Pantazis, D. A. *Faraday Discuss.* **2011**, *148*, 229.
(93) Sinnecker, S.; Neese, F.; Noodleman, L.; Lubitz, W. *J. Am. Chem. Soc.* **2004**, *126*, 2613.
(94) Sinnecker, S.; Neese, F.; Lubitz, W. *J. Biol. Inorg. Chem.* **2005**, *10*, 231.
(95) Amos, A. T.; Hall, G. G. *Proc. R. Soc. London, Ser. A* **1961**, *263*, 483.
(96) Vogiatzis, K. D.; Klopper, W.; Mavrandonakis, A.; Fink, K. *ChemPhysChem* **2011**, *12*, 3307.
(97) Horner, O.; Anxolabéhère-Mallart, E.; Charlot, M. F.; Tchertanov, L.; Guilhem, J.; Mattioli, T. A.; Boussac, A.; Girerd, J. J. *Inorg. Chem.* **1999**, *38*, 1222.
(98) Teutloff, C.; Schäfer, K. O.; Sinnecker, S.; Barynin, V.; Bittl, R.; Wieghardt, K.; Lendzian, F.; Lubitz, W. *Magn. Reson. Chem.* **2005**, *43*, S51.
(99) Schäfer, K. O.; Bittl, R.; Lendzian, F.; Barynin, V.; Weyhermüller, T.; Wieghardt, K.; Lubitz, W. *J. Phys. Chem. B* **2003**, *107*, 1242.
(100) Parsell, T. H.; Behan, R. K.; Green, M. T.; Hendrich, M. P.; Borovik, A. S. *J. Am. Chem. Soc.* **2006**, *128*, 8728.
(101) Hillier, W.; Messinger, J. In *Photosystem II. The Light-Driven Water:Plastoquinone Oxidoreductase*; Wydrzynski, T., Satoh, K., Eds.; Springer: Dordrecht, The Netherlands, 2005; Vol. *22*, p 567.
(102) Dau, H.; Haumann, M. *Biochim. Biophys. Acta, Bioenerg.* **2007**, *1767*, 472.
(103) Klauss, A.; Haumann, M.; Dau, H. *Proc. Natl. Acad. Sci. U.S.A.* **2012**, *109*, 16035.
(104) Mattioli, G.; Risch, M.; Amore Bonapasta, A.; Dau, H.; Guidoni, L. *Phys. Chem. Chem. Phys.* **2011**, *13*, 15437.
(105) Auger, N.; Girerd, J. J.; Corbella, M.; Gleizes, A.; Zimmermann, J. L. *J. Am. Chem. Soc.* **1990**, *112*, 448.
(106) Sarneski, J. E.; Thorp, H. H.; Brudvig, G. W.; Crabtree, R. H.; Schulte, G. K. *J. Am. Chem. Soc.* **1990**, *112*, 7255.
(107) Pal, S.; Chan, M. K.; Armstrong, W. H. *J. Am. Chem. Soc.* **1992**, *114*, 6398.
(108) Siegbahn, P. E. M. *Chem.—Eur. J* **2008**, *14*, 8290.
(109) Siegbahn, P. E. M. *Acc. Chem. Res.* **2009**, *42*, 1871.
(110) Siegbahn, P. E. M. *Phys. Chem. Chem. Phys.* **2012**, *14*, 4849.
(111) Yano, J.; Kern, J.; Sauer, K.; Latimer, M. J.; Pushkar, Y.; Biesiadka, J.; Loll, B.; Saenger, W.; Messinger, J.; Zouni, A.; Yachandra, V. K. *Science* **2006**, *314*, 821.
(112) Pushkar, Y.; Yano, J.; Glatzel, P.; Messinger, J.; Lewis, A.; Sauer, K.; Bergmann, U.; Yachandra, V. *J. Biol. Chem.* **2007**, *282*, 7198.
(113) Barber, J.; Murray, J. W. *Philos. Trans. R. Soc., B* **2008**, *363*, 1129.
(114) Ferreira, K. N.; Iverson, T. M.; Maghlaoui, K.; Barber, J.; Iwata, S. *Science* **2004**, *303*, 1831.
(115) Sproviero, E. M.; Gascon, J. A.; McEvoy, J. P.; Brudvig, G. W.; Batista, V. S. *J. Chem. Theory Comput.* **2006**, *2*, 1119.
(116) Sproviero, E. M.; Gascon, J. A.; McEvoy, J. P.; Brudvig, G. W.; Batista, V. S. *Curr. Opin. Struct. Biol.* **2007**, *17*, 173.
(117) Sproviero, E. M.; Gascon, J. A.; McEvoy, J. P.; Brudvig, G. W.; Batista, V. S. *J. Am. Chem. Soc.* **2008**, *130*, 6728.
(118) Rapatskiy, L.; Cox, N.; Savitsky, A.; Ames, W. M.; Sander, J.; Nowaczyk, M. M.; Rögner, M.; Boussac, A.; Neese, F.; Messinger, J.; Lubitz, W. *J. Am. Chem. Soc.* **2012**, *134*, 16619.
(119) Dau, H.; Grundmeier, A.; Loja, P.; Haumann, M. *Philos. Trans. R. Soc., B* **2008**, *363*, 1237.